**THE EUROPEAN
PHYSICAL JOURNAL B**

Colloquium

Time scale bridging in atomistic simulation of slow dynamics: viscous relaxation and defect activation

A. Kushima[1,2], J. Eapen[3,4,a], Ju Li[2], S. Yip[1,5], and T. Zhu[6]

[1] Department of Nuclear Science and Engineering, Massachusetts Institute of Technology, Cambridge, 02139 Massachusetts, USA
[2] Department of Materials Science and Engineering, University of Pennsylvania, Philadelphia, 19104 Pennsylvania, USA
[3] Department of Nuclear Engineering, North Carolina State University, Raleigh, 27695 NC, USA
[4] Center for Advanced Modeling and Simulation, Idaho National Laboratory, Idaho Falls, 83415 ID, USA
[5] Department of Materials Science and Engineering, Massachusetts Institute of Technology, Cambridge, 02139 Massachusetts, USA
[6] Woodruff School of Mechanical Engineering, Georgia Institute of Technology, Atlanta, 30332 GA, USA

Abstract. Atomistic simulation methods are known for timescale limitations in resolving slow dynamical processes. Two well-known scenarios of slow dynamics are viscous relaxation in supercooled liquids and creep deformation in stressed solids. In both phenomena the challenge to theory and simulation is to sample the transition state pathways efficiently and follow the dynamical processes on long timescales. We present a perspective based on the biased molecular simulation methods such as metadynamics, autonomous basin climbing (ABC), strain-boost and adaptive boost simulations. Such algorithms can enable an atomic-level explanation of the temperature variation of the shear viscosity of glassy liquids, and the relaxation behavior in solids undergoing creep deformation. By discussing the dynamics of slow relaxation in two quite different areas of condensed matter science, we hope to draw attention to other complex problems where anthropological or geological-scale time behavior can be simulated at atomic resolution and understood in terms of micro-scale processes of molecular rearrangements and collective interactions. As examples of a class of phenomena that can be broadly classified as materials ageing, we point to stress corrosion cracking and cement setting as opportunities for atomistic modeling and simulations.

1 Introduction

Computational science, meaning the use of advanced computational methods to solve complex problems, has emerged in recent years to be a highly interdisciplinary field of science and engineering. In the context of condensed-matter research, computational science encompasses computational physics and computational chemistry, both well-established, as well as computational materials science [1] – a relatively new area which is rapidly gaining attention. Computational science plays a synergistic role in connecting traditionally distinct disciplines. This is quite evident in materials research where the coupling of conceptual models and simulations across a wide range of spatial and temporal scales is becoming increasingly pervasive [2–4].

A longstanding goal in multiscale materials modeling and simulation is to probe the atomic-level mechanisms that govern system-level behavior on macroscopic time scales [5,6]. Our aim in the present perspective is to describe such a challenge in two case studies: viscous

relaxation in glassy liquids, a problem of temperature-dependent stress fluctuations, and structural deformation in solids, a problem of stress relaxation and defect dynamics. Both phenomena involve tracking the system evolution over time periods comparable to laboratory experiments and even beyond. It is widely known that for these problems the standard method of atomistic simulation, namely, molecular dynamics (MD), is unable to cope with the slow dynamics, a constraint which has to do with the microscopic time-steps intrinsic to MD, relative to anthropological or geological-scale time behavior. By slow dynamics, we have in mind, the dynamical processes associated with a system that gets trapped from time to time in deep local energy minima and which exhibits long relaxation times. On the other hand, one does not want to give up the detailed molecular configurations associated with the system evolution, since access to such information can be essential to gaining insights into the underlying atomistic mechanisms. The desire for an atomistic method capable of reaching macro time scale, therefore, has motivated the development of a number of simulation techniques, among them, hyperdynamics [7] and

[a] e-mail: `jacob.eapen@ncsu.edu`

metadynamics [8–10] – methods designed to accelerate the sampling of rare events. By the use of history-dependent bias potentials, metadynamics can enable an efficient sampling of the potential energy landscape leading to the determination of the activation barriers and the associated rate constants through the transition-state theory (TST). In this perspective we will describe adaptations of this class of methods to investigate glassy dynamics [11–13], and deformation and relaxation behavior in solids [14–16], and diffusion [15,17,18].

In the study of glassy dynamics our main focus is to provide a theoretical explanation of the temperature variation of the shear viscosity of supercooled liquids [19–21]. The super-Arrhenius behavior of the so-called "fragile" liquids has remained an outstanding issue for the understanding of the glass transition. We find that the transition state pathway (TSP) trajectories sampled by the autonomous basin climbing (ABC) algorithm [11,12] provide sufficient details on the local energy minima and saddle points to allow a semi-quantitative interpretation of the experiments [22] as well as providing insights to a few universal characteristics of "glass fragility" [23,24].

In the study of stress/creep relaxation in deformed solids we trace out the TSP trajectories and time evolution of the system to investigate the underlying atomistic displacement mechanisms. Our simulations reveal discrete, localized atomic displacements such as diffusive motions [15,17,18] or surface dislocation nucleation [16] which appear to be unit processes that may or may not be observed in normal molecular dynamics simulations at strain rates many orders of magnitude higher [25]. As we discuss in the next section, very disparate physical problems display generic features on the potential energy landscape. Landscape sampling, followed by evaluation of transition states and rate constants, allows extraction of the underlying slow dynamical characteristics.

The paper is organized as follows. In Section 2 we briefly survey the current methods for sampling energy landscapes and transition state pathway trajectories. In Section 3 we describe an algorithm, autonomous basin climbing, that is a version of the biased potential method known as metadynamics, and show how TSP trajectories are used to construct an effective or coarse-grained activation barrier $Q(T)$. In Section 4 we describe two methods for estimating the viscosity $\eta(T)$ of supercooled liquids – a heuristic method using $Q(T)$, and a network model formulation based on linear response theory. Experimental tests are presented to bring out new insights concerning strong and fragile glass-forming liquids. In Section 5 we discuss entropy corrections through the Adam-Gibbs model to get an improved estimate of the free energy. In Section 6 we discuss the concepts of activation volume and activation entropy, measures of the stress and temperature dependence of $Q(T)$, and their roles in quantifying the rate sensitivity in the kinetics of defect nucleation and mobility in crystals. We have developed an associated computational method called the strain-boost simulation [16] that uses the Eshelby transformation strains [26] of embedded atomic clusters of certain size as boost variables,

so one could "dial in" the activation volume. We contrast other techniques such as the free-end nudged elastic band (NEB) method [27,28] and hyperdynamics [7], and also note the similarity between the Meyer-Neldel compensation rule and the Adam-Gibbs model. In Section 7 we discuss how ABC sampling method can be used to investigate the diffusional stress relaxation in stressed solids. Lastly in Section 8 we present an outlook that considers several problems of slow dynamics in the area of materials ageing.

2 Energy landscape concepts and transition state theory methods

The atomistic processes that underpin the viscous relaxation in glassy materials and defect mobility in solids are often slow relative to the vibrational timescales of the systems. Thus theoretical and simulation methods that describe such slow or infrequent events [29,30] take advantage of this separation of timescales. Goldstein in 1969 [31] visualized the slow evolution of dynamical systems over a potential energy landscape or surface (PEL/PES) which for an N-particle system is represented by the potential energy function $U(\mathbf{r})$ embedded in a $(3N+1)$ dimensional hyperspace [29,32]. The $3N$ dimensional PEL is often rugged and is decorated with an inordinately large number of minima and saddle points in most systems of scientific and engineering interest. Stable or metastable systems are defined by the local minima given by $\nabla U = 0$ with all the eigenvalues of the Hessian matrix $\nabla\nabla U$ positive.

In the formal treatment of Stillinger and Weber [33,34], the local minima, known as inherent structures (IS), are surrounded by potential energy basins that upon local minimization will map onto the corresponding inherent structures (see Fig. 1). While the PEL is itself temperature independent, the configurational space mostly explored is strongly temperature dependent. Under thermal equilibrium, the system traverses from one basin to another with a rate that is dependent on the energy barrier between inherent structures as well as the temperature. Figure 2 shows a schematic of true and inherent structure trajectories with the former portraying conspicuous vibrational motion at the two prominent basins. Under driven conditions, the rate of escape from the basins is further dependent on the external driving forces which we will discuss more in Section 7.

The formalism of inherent structures, and more generally the energy landscape, provides a unified framework for computing *thermodynamic* and *dynamic* properties of a system. Statistical mechanics delineate the relationship between free energy, and hence, all the thermodynamic properties, to the corresponding partition function. For systems that do not have any significant symmetries such as glasses, the system partition function can be approximated as the sum of basin partition functions [35]. For a canonical ensemble (N, V, T), the system free energy (F) then can then be written as [35]

$$F(T, V) = -TS_{conf}(\langle E_{IS}\rangle) + F_{basin}(\langle E_{IS}\rangle, T, V) \quad (1)$$
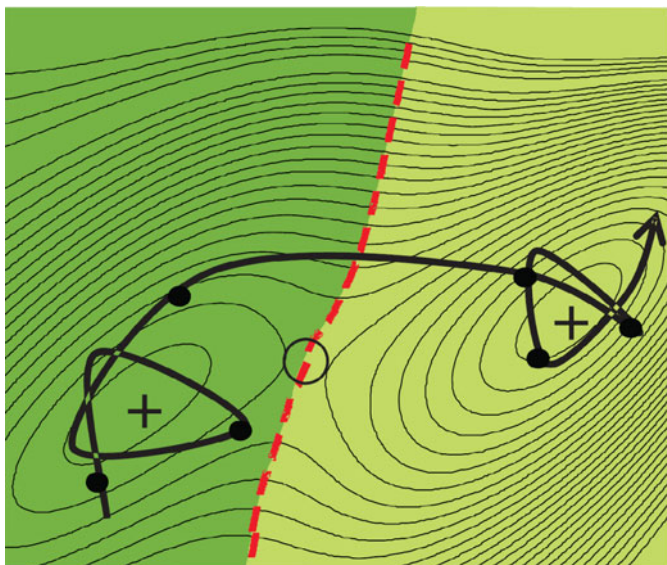
Fig. 1. Schematic of a PEL. The crosses denote the inherent structures (IS) or local energy minima found by energy minimization (steepest descent). The solid line denotes a possible state-to-state trajectory between two minima. Reproduced from [29].
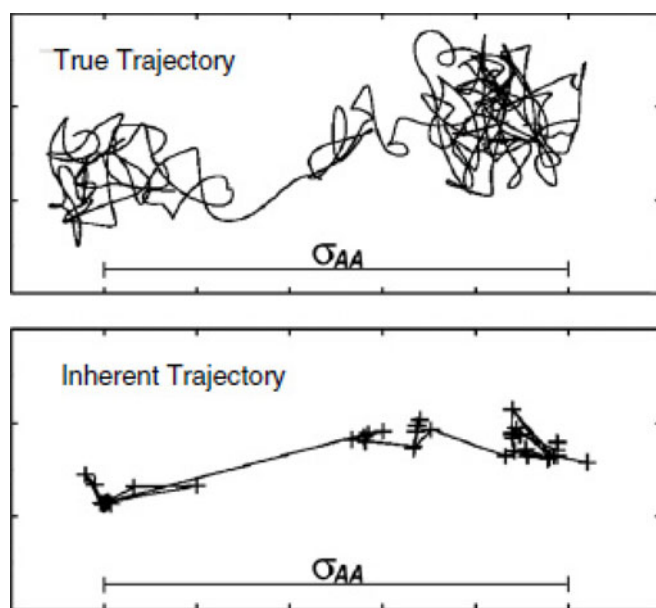
Fig. 2. Schematic illustration of the distinction between an actual (true) trajectory as determined by a molecular dynamics simulation (top panel) and the corresponding trajectory in the inherent structure (IS) description (bottom panel). Reproduced from [29].

where F_{basin} represents the basin free energy, S_{conf} – the configuration entropy and E_{IS} – the inherent structure potential energy. Thus, the system free energy is composed of an entropic term that arises from the multiplicity of inherent structures and a free energy which is characteristic of the energy landscape (denoted by the angular

brackets). The idea of a temperature-dependent characteristic energy $\langle E_{IS} \rangle$ is exploited in our work on computing viscosity of supercooled liquids (Sects. 4 and 5). Note that when the system volume changes, the PEL also changes. Experiments which are usually performed at constant temperature and pressure, therefore, are best analyzed through the enthalpic landscape which corresponds to the (N, P, T) ensemble. When the thermal energy and pressure-volume work contributions are small, as in many applications, system free energy becomes dominated by the potential energy.

Once the free energy of a system is known, all the thermodynamic properties of the system can be calculated. As evident from equation (1), the thermodynamic properties are functions of the average inherent structure energy. Monte Carlo [2] with importance sampling are established methods for sampling the potential energy landscape very efficiently. In particular, umbrella sampling [36], local elevation [37], parallel tempering [38] and adaptive force bias [39,40] are cleverly designed algorithms to accelerate the barrier crossings in a PEL. In another scheme, Wang and Landau [41] proposed to generate the multiplicity of states for a given energy E, $g(E)$, to determine the canonical partition function, and hence all the thermodynamic properties. A key step in the Wang and Landau algorithm is to continuously update $g(E)$ as the simulation progresses. While detailed balance is not satisfied at all steps, the algorithm is very efficient for sampling $g(E)$ directly.

Molecular dynamics with biased potentials can also be performed to accelerate the sampling of rare events on the PEL. Grubmüller [42] devised a conformational flooding algorithm where multivariate Gaussians are introduced in the potential functions. The purpose of this flooding potential is to modify the free energy landscape to encourage the system to hop over the potential energy barriers. The flooding potentials are short ranged such that the barriers themselves do not interact with each other. The essential idea is to construct a coarse grained description that is assumed to be involved with the conformational motion. The free energy and the thermodynamic properties thus become solely based on the coarse-grained description.

Single-point sampling of PEL gives the energy minima but generally does not include any dynamical information from the sequence of sampled configurations. Transition state theory is a theoretical framework which can extract dynamical information by accessing the rate of escape from one inherent structure to another. Originally developed by Eyring [43] for gas-phase reactions and later formulated by Vineyard [44] for solid-state systems, the rate of transition from basin A to an adjacent basin B is approximated by

$$k_{A \to B} = \sum_{A \to B\ MEPs} \frac{\prod\limits_{all\ modes\ i} \nu_i^A}{\prod\limits_{all\ modes\ i\ except\ MEP} \nu_i^{saddle}}$$

$$\times \exp\left(\frac{E_A - E_{saddle}}{k_B T} \right) \qquad (2a)$$

where one sums over all dividing surfaces (saddle points) directly connecting basin A with adjacent basin B. The minimum energy path (MEP), $\mathbf{r}(s)$, is a continuous path in $3N$ dimensional space that goes through the saddle point, where $ds \equiv (d\mathbf{r} \cdot d\mathbf{r})^{1/2}$ is the differential path length, that connects A and B by steepest descent via the corresponding saddle point. It can be shown that the MEP line tangent approaches a normal mode near minima A and B (the inherent structures) and near the saddle point. However, near minima A and B, the normal mode frequency is real, while the normal mode frequency is imaginary near the saddle point. If a single saddle point is dominant in (2a) sum, a lumped frequency factor

$$\nu \equiv \frac{\displaystyle\prod_{all\ modes\ i} \nu_i^A}{\displaystyle\prod_{all\ modes\ i\ except\ MEP} \nu_i^{saddle}}$$

$$\equiv \nu_{MEP} \frac{\displaystyle\prod_{all\ modes\ i\ except\ MEP} \nu_i^A}{\displaystyle\prod_{all\ modes\ i\ except\ MEP} \nu_i^{saddle}} \qquad (2b)$$

is often defined, such that the rate can be expressed in the more familiar form

$$k_{A\to B} = \nu \exp\left(-\frac{\Delta E}{k_B T}\right), \qquad (2c)$$

where ΔE is the saddle point energy relative to the basin A. In (2b), ν_{MEP} is the normal mode frequency along the MEP line tangent at A: it is a physical attempt frequency along the MEP, typically of the order of the Debye frequency ($10^{12}/$s). However, the lumped product ν in (2b) and (2c) can take on a great range of values, from somewhere near the Debye frequency ($10^{12}/$s), to as high as $10^{36}/$s [45] that is faster than any physical timescale of the system, due to a large activation volume (see Sect. 6). Unlike thermodynamic quantities which depend mostly on the inherent structure energies, dynamical quantities are dependent on the potential energy barriers ΔE and vibrational free energy barriers (reflected in ν) that describe the *connectivity* of the inherent structures.

Methods that can determine the saddle point(s) and the MEP(s) between two basins fall into two categories. In the first one, methods such as NEB [27] converge to an MEP with two known basins. Methods such as dimer [46] and activation relaxation technique (ART) [47], on the other hand, can predict nearby inherent structures as well as the best estimate for the transition pathway between them. We briefly describe ART which was proposed by Barkema and Mousseau [47] for simulating energy-minimized structures specifically for glasses. In the first ART step, the configuration is moved (activated) to the local saddle point, and in the next, it is relaxed to the new minimum. First a single atom is displaced along a random direction and then the configuration is forced to climb to the nearby saddle point through an iterative approach using Levenberg-Marquardt (LM) extremization [48] which is a mixture of steepest-descent and second order Hessian evaluation. A cluster or all atoms can be forced to move collectively at the beginning, but they generate several spatially separated events which then become difficult to disentangle. Hence, a single atom displacement is usually preferred. A direct LM implementation is expensive for large systems. Barkema and Mousseau have computed a local Hessian which contains only the 3×3 blocks along the diagonal of the full Hessian and have reported fairly good accuracy. Note that there are no general methods that can locate all the saddle configurations around a minimum. In this respect, different methods such as dimer and ART can potentially give different saddle point configurations depending on the physical system.

In the hyperdynamics formulation of Voter [7], a non-negative bias potential $\Delta U(\mathbf{r})$ is added to the original potential surface $U(\mathbf{r})$. Assuming TST holds and there are no correlated events, hyperdynamics preserves the correct Markovian branching statistics of state-to-state (IS–IS) evolution with the modified potential. Significant acceleration or boost can be obtained which is a function of the biased potential that is set to zero at the dividing surface (between two basins) to be compliant with TST. In the original formulation, a Hessian based technique was employed for constructing the biased potential which was found to be computationally expensive. Local bias potentials such as the bond-boost method [49] and the strain-boost method [16] have been shown to be computationally less expensive in subsequent investigations. In recent years, hyperdynamics have been reformulated to work on entropic barrier problems where naive TST is not applicable [50].

Metadynamics [8–10,51] is an approach that utilizes the idea of coarse or collective variables which are functions of the system configuration ($\mathbf{r}$) that have a reduced dimensionality [52,53], along with the idea of Grubmüller's conformational flooding [42], and the algorithm of Wang and Landau [41]. In this algorithm, the properly identified collective variables, such as the potential energy of the system [54–56], evolve in time under a history-dependent potential which is generally constructed as a sum of Gaussians along a trajectory [8–10,51]. Gaussians modify the PEL as the simulation progresses and enable the system to overcome the energy barriers and sample the PEL very efficiently. Originally developed to reconstruct the underlying free-energy landscape of a system, it can be also used as a transition-state pathway sampling technique to determine saddles, transition states and rate constants.

The most distinguishing feature of metadynamics is the way in which the external bias potential is formulated. This potential is history-dependent in that the bias at any step in sampling depends on the previous part of the trajectory that is being sampled [57]. For recent reviews of the theory, formulation of collective variables, and chemical and biomolecular applications of metadynamics, see references [9,10].

3 Transition state pathway (TSP) sampling with ABC algorithm

In this section we discuss an adaptation of metadynamics [8–10,51,57] to calculate the shear viscosity of deeply cooled liquids [11]. For sampling the potential energy landscape, the algorithm employs a series of activation-relaxation steps. Suppose the system initially lies in a local minimum energy state. An activation step is first applied by imposing an energy penalty function, chosen to be a Gaussian [8–10], followed by a relaxation step in which the entire system is relaxed by energy minimization. The cycle is repeated until the system finds itself in a new local minimum as depicted in Figure 3.

The ABC algorithm comprises of the following six steps [11]. In Step 1, an initial structure corresponding to a local energy minimum is selected. An energy penalty function Φ_P^k is then added to the original potential U in Step 2, $\Phi_P^K = U + \sum_{k=1}^{K} \Phi_P^k$ ($K = 1$, initially), followed by minimization of the modified potential Φ_P^K in Step 3. During the minimization process, the center of mass of the system is fixed to prevent any drift. In our simulations, a Gaussian $\Phi_P^k(\mathbf{r}) = W \exp\left[-(\mathbf{r} - \mathbf{r}_{min}^k)^2/2\sigma^2\right]$ is chosen as the energy penalty function, with $\mathbf{r}_{min}^k$ as the relaxed atomic configurations at the kth energy minimization step. The parameters W and σ are constants which determine the strength and the width of the Gaussian, respectively. Steps 1–3 are then repeated, with the penalty function accumulated, until a new local minimum is detected in Step 4. Note that if the system does not climb out of the local energy basin, there will be a difference between original potential U and the modified potential at $\mathbf{r}_{min}^k$. Thus a new IS is identified when the difference vanishes, along with the criterion $\nabla U = 0$. Notice that the PES which is modified is not a static quantity, but rather it evolves along the sampling trajectory. So long as the penalties are not removed during the sampling, the system is discouraged from returning to any of the local minima previously visited. Henceforth we dub this algorithm autonomous basin climbing (ABC) for its ability to sample complex potential energy landscapes and escape steep basins through cumulative addition of energy penalty function $\left(\sum \Phi_P^k\right)$.

In Step 5, the saddle-point energy and the corresponding atomic configurations are found by backtracking along the energy minimization path. Though approximate, this method gives reasonable saddle configuration and energy. The ABC algorithm has been tested on a problem of atomic diffusion on a metal surface [58] for which known results are available [7,59,60]. This test is instructive for optimizing the choice of the Gaussian width σ and height of the penalty function W [11]. The ABC algorithm is shown to correctly predict the knock-out mechanism of surface diffusion in a single run which is significantly faster than comparable methods. And finally in the last step, Steps 1–5 are repeated until sufficiently large tracts of potential energy landscape is sampled. Algorithmic improvements can be made on the sampling technique by combining ABC algorithm with methods such as parallel
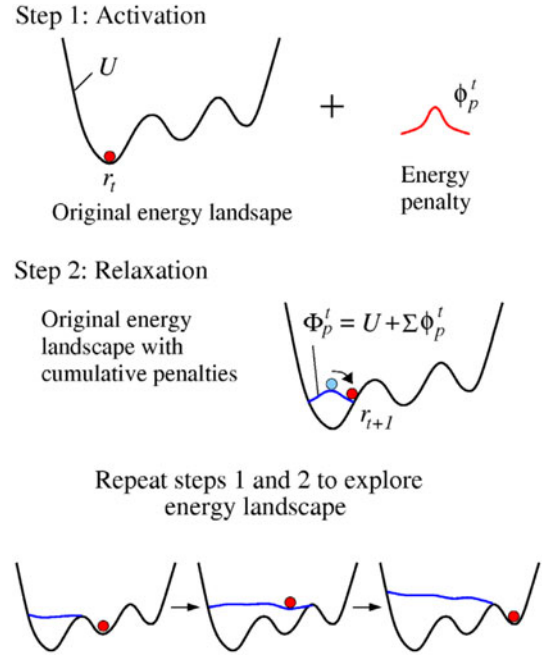
Fig. 3. Schematic illustration of potential energy landscape sampling in the metadynamics/ABC algorithm. Original potential and the modified potential with penalty functions are denoted by U and Φ_P^K, respectively. A cumulative penalty function $\sum \Phi_P^k$ is imposed at each step in the activation-relaxation sequence. As depicted, the system is first pushed out of the first potential energy basin by the cumulative penalty function, into the second by crossing the lowest saddle barrier. The process is repeated as the system proceeds to visit the neighboring energy basins. Reproduced from [14].

tempering [10,38], along with identifying the saddle points through techniques such as nudged elastic band (NEB) method [27].

In Figure 4, we show the energy minima and energy barriers of a system of 100 atoms interacting through a binary Lennard-Jones (BLJ) potential model [61,62] sampled with the ABC algorithm [11]. This system has been earlier investigated for its slow viscous response [11]. The binary alloy consists of two types of atoms (A and B) with the concentration ratio A:B = 4:1. The interaction between atoms α and β is described by $u_{\alpha\beta}(r) = 4\varepsilon_{\alpha\beta}[(\sigma_{\alpha\beta}/r)^{12} - (\sigma_{\alpha\beta}/r)^6]$, where $\varepsilon_{AA} = 1.0$, $\varepsilon_{AB}/\varepsilon_{AA} = 1.5$, $\varepsilon_{BB}/\varepsilon_{AA} = 0.5$, $\sigma_{AA} = 1.0$, $\sigma_{AB}/\sigma_{AA} = 0.8$, and $\sigma_{BB}/\sigma_{AA} = 0.88$. The potential is truncated and shifted to 0 at $2.5\sigma_{\alpha\beta}$. The parameters of the penalty function takes the values, $W = 1.0$ and $\sigma^2 = 0.1$. As shown in Figure 4, the trajectory is an open-ended sequence of alternating minima and saddle points, each of which is determined by a series of activation-relaxation steps described earlier. The irregularity of the fluctuations in the trajectory, and the appearance of well-separated metabasins indicate a rough energy landscape that is associated with fragile materials [21]. From such data one can construct other forms of PES representations. For example, disconnectivity graphs [63] and tree diagrams [32], have been used to describe the connectivity of the local minima through the
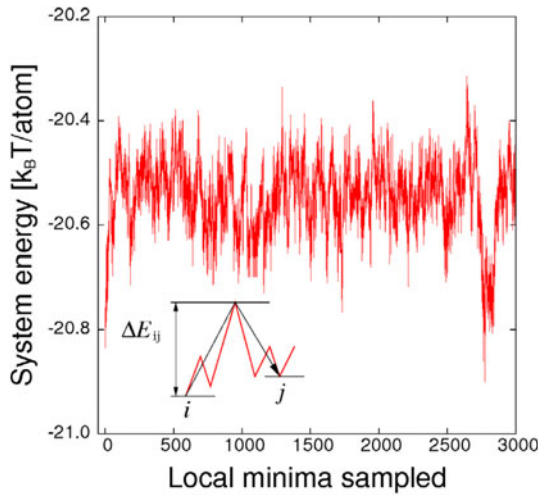
Fig. 4. A TSP trajectory for the BLJ supercooled liquid state [61,62] generated by the ABC algorithm. The inset shows the definition of the activation barrier ΔE_{ij} as the system escapes from inherent structure i to inherent structure j, as $\Delta E_{ij} \equiv E_s - E_i$ where E_s is the energy of the characteristic saddle point configuration between i and j, and E_i is the energy of state i. The ABC algorithm generally evaluates the lowest saddle between i and j. This is the essential output of the simulation that is used to estimate the structural relaxation time, and hence, the shear viscosity of the system. Also note that $\Delta E_{ij} \neq \Delta E_{ji}$. Reproduced from [11].

saddle points. For the trajectory shown in Figure 4, the corresponding disconnectivity graph and potential profile are given in Figure 5. The profile is consistent with our previous observation on the roughness of the underlying energy landscape.

Relative to the original formulation of metadynamics [8] the ABC algorithm is different in the following aspects in its initial development and application to supercooled liquids [11–13]. In ABC the bias potential acts on *all* the atomic degrees of freedom in the system. Clearly one can also apply the potential only to a subset of degrees of freedom (see, for example, the ad-atom diffusion benchmark study in Ref. [11]). The formulation of collective variables in metadynamics has been extensively discussed recently [10]. It is noted that the self-accumulated boost potential can be applied continuously to collective variables during an MD simulation through a Lagrangian formulation or by acting directly on the microscopic coordinates of the system. In the ABC implementations discussed here, the bias potential is used in energy minimization calculations as opposed to dynamic simulations. This too is not an inherent limitation. In the outlook section we will comment further on the relations between ABC and other sampling methods currently in use.

# 4 Shear viscosity of supercooled liquids: fragile temperature scaling

Abundant experimental data exist that show a sharp increase in the shear viscosity of glassy liquids, $\eta(T)$,
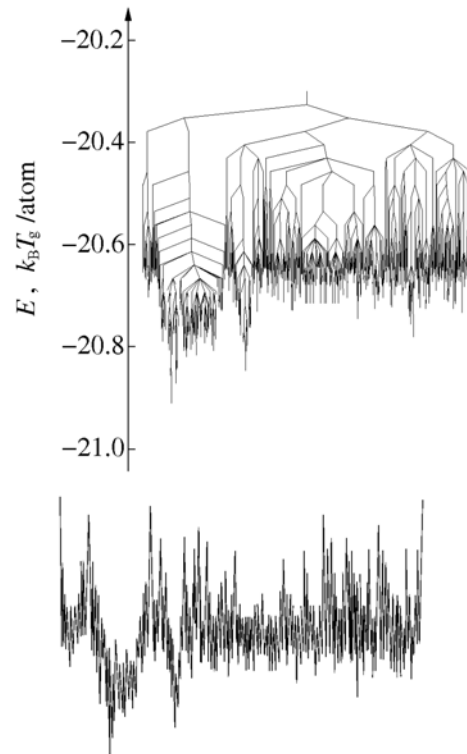
Fig. 5. Disconnectivity graph [12] of a supercooled liquid described by a binary Lennard-Jones potential model [61,62] (upper) and corresponding potential energy profile [12] (lower). The topographical features of the disconnectivity graph indicate a rough potential energy landscape. Reproduced from [12].

over a small range of temperature decrease [19–21]. Explaining this super-Arrhenius behavior in terms of intermolecular interactions, on the other hand, is a long-standing challenge. A topic which is still of current interest is the origin of "glass fragility", the onset of super-Arrhenius temperature dependence in certain glass-forming liquids [19,21,29,64]. To address this issue we have applied the ABC sampling technique to obtain TSP trajectories in simple liquids that have been quenched to temperatures in the supercooled region, and calculated $\eta(T)$ using the statistical information on local energy minima and saddles from the trajectories. Two approaches were developed, both involving TSP trajectories as input. One is a heuristic approach in the spirit of transition-state theory where $\eta(T)$ is governed by a temperature-dependent activation barrier $Q(T)$ which is constructed from the TSP trajectories. The other is a modification of the Green-Kubo linear response theory where the stress correlation function is obtained from the solution to a master equation in which the transition probability is specified by the TSP trajectories. Using the $Q(T)$ formulation the temperature variations of $\eta(T)$ has been predicted for two models of intermolecular interaction, one appropriate for fragile liquids and the other for strong liquids. As we will see below fragile versus strong temperature scaling characteristics can be given a unified interpretation. The modified Green-Kubo formulation gives results for fragile liquids
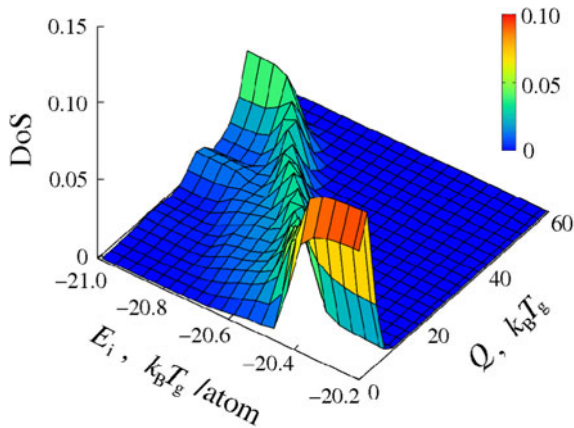
Fig. 6. Density of states surface in the plane of the two variables, the activation energy Q and the well depth of a local energy minimum, in the statistical analysis of the TSP trajectory shown in Figure 4. The "ridge" on this surface traces out a Q-E_{IS} correlation (in the sense of high probability) that goes into making up of the temperature-dependent activation barrier (the single-path approximation). Reproduced from [11].

that can be benchmarked against direct molecular dynamics simulation in the high temperature range, and results in the low temperature range that can be compared to experiments.

The coarse-grained activation barrier $Q(T)$ is constructed by performing a statistical analysis of the TSP trajectory data shown in Figure 4. We discuss here only the basic idea of the coarse graining and leave the details to the original work [11]. The analysis begins with defining the activation free energy required to go between an arbitrary pair of local energy minima, as resembled by ΔE_{ij} in Figure 4. In an ensemble of sampled trajectories, the value ΔE_{ij} is not unique statistically speaking, because there can be different pairs of minima connected by essentially the same *value* of activation energy. Such degeneracy applies also to the energy of the initial local minimum; there can be a number of E_j^m having the same value, say E_i. By considering all possible ways of connecting pairs of local minima, we generate from Figure 4, a two-dimensional surface (density of states) in the variables Q and E_i. This result is shown in Figure 6.

One sees on this surface a "ridge" of high density of states, the projection of which onto the Q-E plane gives a function $Q(E_{IS})$. Physically $Q(E_{IS})$ describes the variation of a coarse-grained (effective) activation energy with the initial inherent structure potential energy of system (see Eq. (1)). Qualitatively one can see that if initially the system is in a relatively shallow local potential energy minimum, only low activation energy is needed for the system to escape. On the other hand, if the system is initially in a deep local minimum, the activation energy then rises considerably. In effect our analysis amounts to constructing the probability distribution, $\rho(Q; E_{IS})$ of the activation energy Q required by the system to escape from its initial state with energy E_{IS}. The first moment of the distribution, $Q(E_{IS})$, is the most probable value which
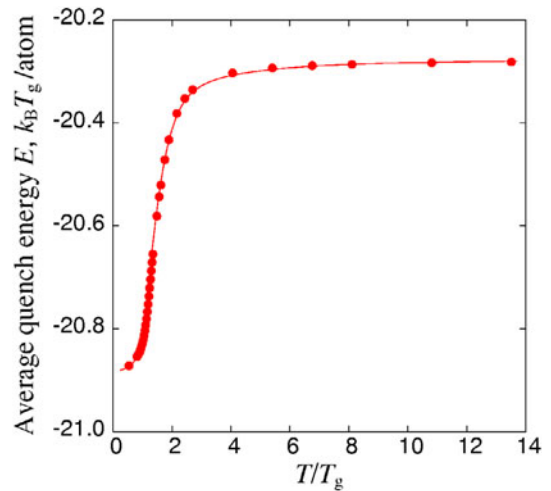

Fig. 7. Variation of average inherent structure potential energy of a quenched liquid with the quench temperature for the binary Lennard-Jones model [61,62], both expressed in terms of the glass transition temperature T_g [11]. Note the sharp decrease in E_{IS} when temperature decreases to the range $T/T_g \sim 2$. This indicates that in a liquid supercooled to temperatures below $2T_g$, the system is likely to encounter significantly deeper energy minima than those encountered at the higher temperatures. Reproduced from [11].

varies with E_i. For the problem of viscosity of supercooled liquids, we seek a coarse-grained activation barrier, $Q(T)$ which depends on the temperature of the supercooled liquid T. We obtain $Q(T)$ from $Q(E_{IS})$ by a variable transformation using a relation from the inherent structure theory of liquids [33]. This relation, shown in Figure 7, is between the energy minima (inherent structure) obtained by quenching the system and the temperature T at which the "quenching" (energy minimization) is initiated. Figure 7 allows every value of E_{IS} in $Q(E_{IS})$ to be replaced by T. The resulting $Q(T)$ is given in Figure 8.

One should notice the simple behavior of the three relations in this analysis $Q(E_{IS})$, $E_{IS}(T)$ and $Q(T)$. We have already mentioned the increase of $Q(E_{IS})$ as the initial local minimum reaches certain depth. Figure 7 shows a characteristic temperature below which the average quench energy becomes sharply lowered. Together these two relations combine to give an activation barrier which is small and constant at high temperatures and rises steeply when temperature is $\sim 2T_g$ and below. Thus the behavior $Q(T)$ has two components, one associated with activated state kinetics (Fig. 6) of overcoming barriers, and the other from the temperature distribution of local energy minima which is thermodynamic in nature (Fig. 7). We now examine the validity of these calculations and check whether such behavior is also seen in other liquid models.

4.1 Green-Kubo theory of linear response: network model and master equation approach

In linear response theory (Green-Kubo formalism) [65,66] transport coefficients of fluids are expressed as integrals of
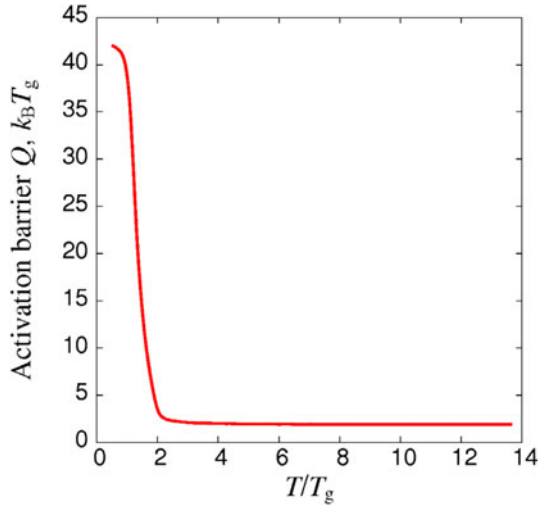
Fig. 8. Temperature-dependent effective activation barrier $Q(T)$ for the binary Lennard-Jones model [61,62] obtained by cross correlation of Figures 6 and 7 [11]. The result shows a striking behavior, low and constant barrier for temperatures above $\sim 2T_g$ and a steep rise to a high barrier (by a factor of about 20) over a narrow temperature range, where it appears to level off. Reproduced from [11].

time correlation functions. The shear viscosity η is given by the time integral

$$\eta(T) = \frac{\Omega}{3k_BT} \int_0^\infty \langle \sigma^{yz}(t)\sigma^{yz}(0) + \sigma^{xz}(t)\sigma^{xz}(0)$$
$$+ \sigma^{xy}(t)\sigma^{xy}(0) \rangle \, dt \qquad (3)$$

where Ω is the volume of the simulation cell maintained at temperature T, and the shear stress tensor is

$$\sigma^{xy} = \frac{1}{\Omega}\left[\sum_j m_j v_j^x v_j^y + \frac{1}{2}\sum_{i \neq j} r_{ij}^x F_{ij}^y\right] \qquad (4)$$

where F is the force between two atoms i and j, r is the position vector and v is the velocity. For simplicity we suppress the superscript xy and introduce the time-dependent shear stress autocorrelation function $S(t) = \langle \sigma(t)\sigma(0)\rangle$. In dense gases and normal liquids $S(t)$ decays on the microscopic time scale of molecular collisions, therefore it can be readily evaluated by molecular dynamics (MD) simulations. In the supercooled regime $S(t)$ no longer decays on the timescale of intermolecular collisions and MD becomes ineffective. To overcome this difficulty we resort to two formulations of activated-state kinetics, both making use of the TSP trajectory data generated by the ABC algorithm. The formulations are not unrelated in that one may be regarded as a limiting case of the other.

Accordingly we follow the Green-Kubo formalism but do not use MD as in previous studies. Instead we analyze $S(t)$ by treating basin hopping as a random walk on a Markov network of nodes [13]. We imagine the system

is able to sample a number of deep minima within the timescale of the calculation, so the average macroscopic properties such as the viscosity can take on steady state values. We also assume the activation barriers for hopping are sufficiently high compared to k_BT, and the energy dissipation sufficiently efficient that after each hop the system loses memory of its previous history. Under these conditions we may take the hopping rate from nodes i to j to be given by harmonic transition state theory,

$$a_{ij} = \nu_0 \exp\left(-Q_{ij}/k_BT\right) \qquad (5)$$

where ν_0 is a characteristic attempt frequency, and Q_{ij} the activation free energy for hopping from state i to state j. In the Markov network model the stress correlation function can be expressed as a sum of contributions, one from each node [13]

$$\langle \sigma(t+\tau)\sigma(t)\rangle = \sum_i P_i \sigma_i g_i(\tau) \qquad (6)$$

where P_i is probability the system is on node i, σ_i is the shear stress on node i, and $g_i(\tau)$ is the expectation value of the shear stress at time $t = \tau$ given that the system was at node i at $t = 0$ (therefore the initial system stress would be σ_i). One may regard $g_i(\tau)$ to be the time-dependent stress propagator for node i. Note that the stress correlation function is the product of σ_i and $g_i(\tau)$ averaged over all i. The calculation of $\eta(T)$ according to equation (3) therefore becomes a matter of evaluating the summation over all nodes as given by equation (6).

Under the assumption that node hopping is a Markov process [67,68] (successive hopping rates are independent of each other), one can set up a "balance" or conservation relation for $g_i(\tau)$ in the form,

$$g_i(\tau) = \int_0^\tau d\tau' s_i(\tau') \sum_j a_{ij} g_j(\tau - \tau') + s_i(\tau)\sigma_i \qquad (7)$$

where $s_i(t) = \exp(-a_i t)$ is the probability that the system will stay at node i during time t, and $a_i = \sum_j a_{ij}$ is the rate at which the system will leave node i. The first term in equation (7) is the contribution to the stress at time τ from the process where the system stays at node i from $t = 0$ to $t = \tau'$, hops to node j at time τ', and evolve further during the interval $\tau - \tau'$. The second term is the contribution from the process where the system remains at node i during the interval τ. Equation (7) is a time integral equation which can be readily solved by Laplace transform. The solution is particularly straightforward because one is interested only in the time integral of the propagator $g_i(\tau)$ as indicated in equation (3). The result is

$$\eta(T) = \frac{\Omega}{k_BT}\sum_i P_i \sigma_i \frac{(\mathbf{A}(\omega = 0^+)^{-1}\boldsymbol{\sigma})_i}{a_i} \qquad (8)$$

where $\mathbf{A}(\omega)$ is the matrix $A_{ij} \equiv \delta_{ij} - \frac{a_{ij}}{\omega + a_j}$ (by definition $a_{ii} \equiv 0$), and $\boldsymbol{\sigma}$ is the vector of inherent stress $(\boldsymbol{\sigma})_i = \sigma_i$. One may regard $\mathbf{A}$ as a dimensionless

frequency-dependent resolvent matrix describing the coupling between nodes with appropriate modulation associated with individual hopping rates. Equation (8), to our knowledge, is a new way of calculating the viscosity in terms of the nodal activation energy Q_{ij} (which specifies a_{ij}), and the energy of the nodes, E_i. In equation (8), σ_i denotes the shear stress at node i and P_i, the canonical probability distribution is given by

$$P_i = \frac{\exp\left(-E_i/k_B T\right)}{\sum\limits_{j} \exp\left(-E_j/k_B T\right)}. \tag{9}$$

Comparing equations (3) and (8) one sees the formulation of the network model effectively replaces the time integral of the stress correlation function by a nodal average of the product of two stresses multiplied by $(a_i)^{-1}$. Since a_i is the rate of leaving node i, its reciprocal is the residence (or relaxation) time of node i. Physically, equation (8) shows the viscosity is essentially the product of a shear modulus and a shear relaxation time.

Equation (8) also provides a basis for a heuristic calculation where one assumes all the activation energies between nodes can be lumped into a single effective activation barrier Q. Consider the special case of a two-state model, where $P_1 = P_2 = 1/2$, $\sigma_1 = -\sigma_2 = \sigma_0$,

$$a_{12} = a_{21} = \nu_0 \exp\left(-Q/k_B T\right).$$

Then equation (8) reduces to

$$\eta = \sigma_0^2 \nu_0^{-1} \exp\left(Q/k_B T\right). \tag{10}$$

This limiting case provides a connection between the network formulation under discussion and a heuristic model to be introduced next.

4.2 Heuristic model of effective activation barrier

Equation (10) is in the form of an expression that has been widely used to analyze experimental data on viscosity [11],

$$\eta(T) = \eta_0 \exp[Q(T)/k_B T]. \tag{11}$$

This expression was first used by Andrade as a two-parameter formula to describe liquid viscosities. The prefactor η_0 and the activation barrier Q were treated as fitting constants. We will use equation (11) in the opposite way. Instead of fitting experimental data we will use equation (11) to calculate the viscosity using the coarse-grained activation barrier $Q(E_{IS}(T))$ which we have just derived earlier in this section (see Fig. 8). We will henceforth refer to this approach the heuristic model of shear viscosity. Equations (8) and (11) are therefore two complementary formulations to calculate $\eta(T)$, with both depending on TSP trajectories as the basic input. Both calculations are predictive in that only a knowledge of the interatomic interaction potential is needed to determine the temperature variation of $\eta(T)$. However, as we will now discuss, for the purpose of testing the numerical results from equation (8)

or (11) against molecular dynamics simulations or experimental data, a normalization is unavoidable because of the prefactor in the hopping rate, the attempt frequency ν_0 in equation (5) needs to be specified. This degree of freedom is rather standard in transition state theory calculations. The normalization amounts to choosing a value for ν_0, or η_0 in equation (11) [11]. We will see that so long as a reasonable value is taken, $\nu_0 \sim 10^{11}$ s^{-1}, the precise value is of no importance.
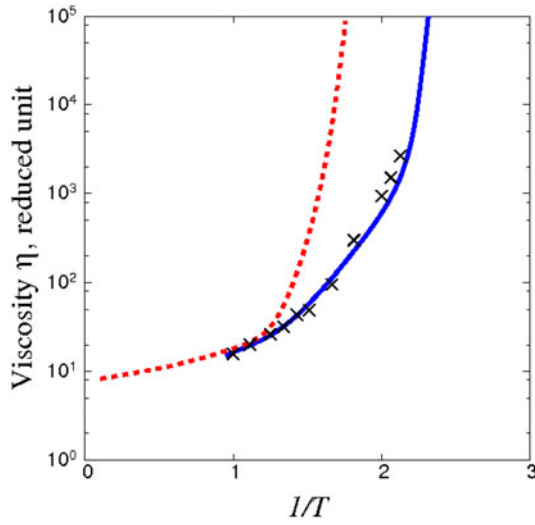
The network model and heuristic formulations will be tested in two ways. The first will be to compare the results with those obtained independently by Green-Kubo molecular dynamics, which is feasible only at low viscosity values (high temperature). Nonetheless, this verification is significant because all the results are calculated using the same interatomic interaction model, so the issue of whether the interaction model is valid therefore does not arise. The second test will be a comparison with experimental data in the intermediate to high viscosity range (1–10^{12} Pa s). In this comparison one needs to keep in mind that the atomistic calculations are performed using the binary Lennard-Jones (BLJ) model potential [61,62] which does not necessarily describe any real liquid. The first test will bring out the accuracy of the two formulations against what is believed to be the correct method of calculation, namely, the molecular dynamics (MD) simulation results, so long as the temperature range is in the region where molecular results are reliable. This is important for appreciating the nature of the heuristic formulation, as a limiting case of the network model formulation. The second test will establish the extent to which the present formulations are able to describe the observed temperature variation of the viscosity of supercooled liquids in the region most relevant to the understanding of the nature of the glass transition. This direct validation has not been previously demonstrated to our knowledge.

4.3 Viscosity at high temperatures: comparison with molecular dynamics simulations

At temperatures near the normal liquid range the viscosity values are low enough for conventional MD to be effective in determining $\eta(T)$ from equation (3). We have performed standard MD simulations using a periodic cubic simulation cell containing 500–2048 atoms. After equilibration is attained, typically in 100 000 time steps, the simulation is allowed to proceed for a buffer period of 10 000 steps without any temperature control. The stress autocorrelation function is then averaged over 2000 sets in the *NVE* ensemble and 8–12 independent runs.

Figure 9 shows the MD results with the viscosity and the temperature expressed in reduced units [11].

In implementing equation (8) we take each local minimum given by the TSP trajectory in Figure 4 to be the energy of a node, and the transition frequency a_{ij} in equation (5) is then specified by the activation barrier ΔE_{ij} as labeled in Figure 4. In implementing equation (11) we take the effective activation barrier $Q(T)$ to be the result
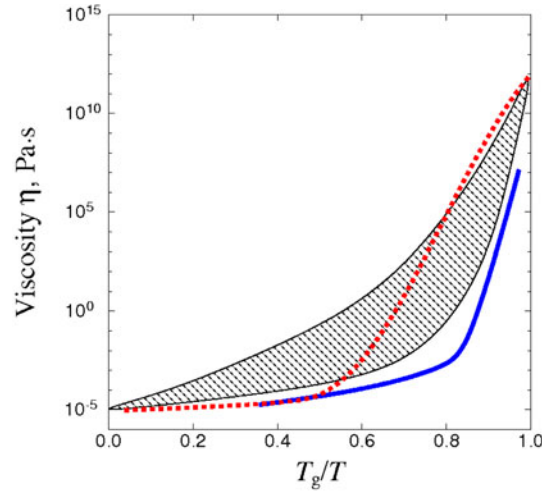
Fig. 9. Benchmarking viscosity results given by the heuristic formulation (dashed line) and network model (solid line) against linear response (Green-Kubo) theory with MD simulations (crosses). All three results are normalized at $T = 1$ (in reduced unit) [11]. MD and network model results are seen to be in close agreement. Overestimate of the activation barrier in the heuristic model can be attributed, at least in part, to the single path approximation (see the discussion of Fig. 6). Reproduced from [11].

Fig. 10. Comparison of temperature variation of calculated and measured shear viscosity (in absolute units) of glass-forming liquids, with T normalized by T_g [11]. Experimental data are represented by the cross-hatched area, and results of the heuristic formulation and network model calculation are indicated by the dashed and solid lines respectively, with all three normalized at a viscosity of 10^{-5} Pa s in the high-temperature limit. For the calculations T_g is taken as 0.37 in reduced unit. Reproduced from [11].

shown in Figure 8. To put the network model and single path approximation results in the form for comparison with MD we normalize all viscosities at $T = 1$. Figure 9 shows that the network model matches well with the MD data. This means our formulation of the Green-Kubo formalism to incorporate activated state kinetics correctly describes the temperature variation of the viscosity as determined by the Newtonian dynamics. In contrast, the heuristic single path approximation (SPA) formulation is seen to give a temperature variation indicating $Q(T)$ is rising too strongly with decreasing temperature. This is actually not surprising given what we have noted about the single path approximation; indeed one should expect $Q(T)$ in Figure 8 to be only an upper-bound estimate. Based on the comparison shown in Figure 9 we attribute the difference between the network model and SPA to arise from the different ways of coarse graining the TSP trajectory inherent in the two formulations.

## 4.4 Viscosity of viscous liquids: calculations and experiments

In comparing the network model and SPA results with experimental data we adopt a different normalization from the preceding comparison with MD. Recall that the normalization amounts to assigning a numerical value to the frequency ν_0 in equation (5), or the prefactor η_0 in equation (11). Given that the experimental data for a number of fragile liquids all extrapolate at high temperature to a viscosity of 10^{-5} Pa s, approximately, (see Fig. 10) it seems
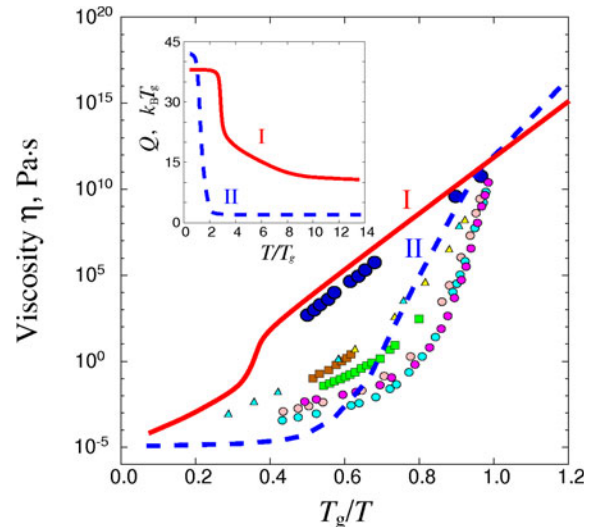
appropriate to use this value as the high-temperature limit in normalizing the network model and SPA results. In Figure 10 the two theoretical results for $\eta(T)$ are now shown in absolute units along with a collection of experimental measurements on fragile liquids [22]. In this figure temperature is scaled against T_g, the glass transition temperature defined operationally as $\eta(T_g) = 10^{12}$ Pa s.

For the experimental data the T_g of each liquid is of course known, while for the two theoretical curves we use the T_g value of 0.37 in reduced unit (temperature at which the SPA model predicts a viscosity of 10^{12} Pa s) [11]. Since there are no other viscosity calculations giving results anywhere near 10^{12} Pa s for the BLJ model (or any interatomic potential for that matter), there is no way to directly validate our value of T_g from a viscosity perspective. From thermodynamic considerations, the Kauzmann temperature, which can be assumed to be close to T_g, of BLJ system is evaluated to be 0.32 approximately [69]. This difference can be resolved by noting that the small size of the system employed with ABC algorithm (employing few hundreds of atoms), generally overestimates relaxation times and hence, the corresponding transport coefficients [70]. There is also an estimate of the mode-coupling theory temperature T_c for the BLJ model, $T_c = 0.435$ [62,71]. This would give a value for the ratio $T_c/T_g \sim 1.2$ which is consistent with a general rule-of-thumb [22]. In comparing the network model and SPA with experimental data on fragile liquids we are primarily interested in understanding the characteristic non-Arrhenius behavior of these liquids. Figure 10 shows the overall comparison, where the range of experimental data is indicated by a shaded band.
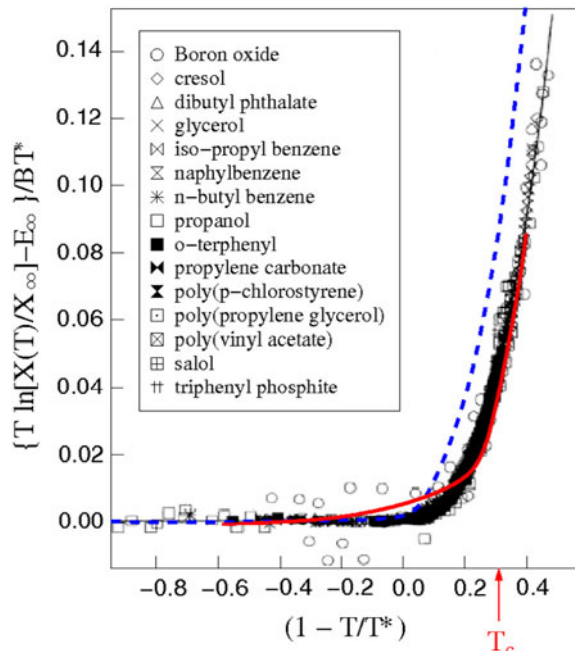
Fig. 11. Comparison of calculations, heuristic formulation (dashed line) and network model (solid line), with experimental data (various symbols), with viscosity and temperature reduced using three parameters to obtain a universal curve [13]. Reproduced from [13].


Fig. 12. Comparison of shear viscosity of liquid silica calculated using the heuristic formulation (solid red curve I) with experimental data [22] (closed blue circles) [12]. Also shown are results for fragile liquids, calculation (dashed curve II) and experimental data (various symbols). Inset shows the corresponding $Q(T)$ for the two liquid models, same format as Figure 8. Reproduced from [12].

In the high-temperature limit $\eta(T)$ starts out to be rather temperature insensitive, and as temperature decreases the viscosity increases gradually until a characteristic temperature is reached. Below this temperature $\eta(T)$ increases in a super-Arrhenius manner. Both the heuristic model and the network model results display this behavior qualitatively, while they differ in the quantitative manner in which the transition from Arrhenius to super-Arrhenius variation occurs. In the heuristic model results the super-Arrhenius behavior sets in too early (overestimate of characteristic temperature) and also somewhat too strongly relative to the experimental band and the network model results. This feature is consistent with what we have seen in the previous test against MD simulations. The extent of the agreement between the network model and experiments may be considered satisfactory given that the interatomic potential model used in the calculations is not known to correspond with any real fragile liquid. The dataset shown in Figure 10 contains 7 liquids. A larger dataset, containing 15 liquids, has been analyzed to extract an effective activation barrier using three scaling parameters. Figure 11 shows the temperature variation of the activation barrier thus extracted. In the limit of high temperature the extracted barrier is scaled to be zero and remains temperature insensitive until T approaches T^* [11,13], one of the three scaling parameters. Below T^* the barrier increases sharply. As a result of the scaling, most of the data points fall onto a universal curve. Results of the heuristic and the network model formulations are also shown in Figure 11, fitted to the

same mathematical form. In this way of comparison the network model is seen to be in quite good agreement with experiments, particularly in the steepness of the activation barrier increase [13].

We have extended the ABC sampling of TSP trajectory, the statistical analysis to determine $Q(T)$, and the calculation of $\eta(T)$ to a potential model for liquid SiO2, which is well-known to be a strong glass former [12]. Figure 12 shows the predicted viscosity compares very well with experiments, both showing a clearly Arrhenius temperature variation in the range where measurements could be made. To contrast this behavior with the super-Arrhenius variation that characterizes the class of fragile liquids, the previous results for the binary Lennard-Jones potential and the experimental data of 7 fragile liquids are plotted again. To see further the origin of the strong versus fragile temperature scaling, the corresponding coarse-grain activation barriers $Q(T)$ for the two potential models are shown in the inset in Figure 12.

Assuming for the moment the theoretical curves are accurate enough, we note that the activation barriers for strong and fragile liquids share a similar structure which is sketched schematically in Figure 13. The essential features of this structure are the limiting values of high and low activation energies at Q_H and Q_L, and a smooth interpolation across an intermediate temperature range bounded by T_L and T_H. The structure depicted in Figure 13 suggests the following physical description. When the system is evolving at temperatures above T_H, it encounters only shallow potential wells and requires only a low activation energy Q_L to sample the energy landscape. As the system is supercooled to below T_H, it becomes increasingly likely to be trapped in deeper potential wells. Correspondingly,
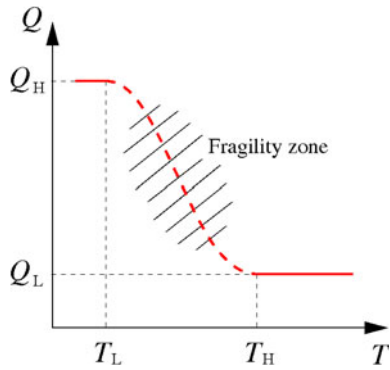
Fig. 13. Schematic of a generic coarse-grained activation barrier with a bi-level structure and a fragility zone [12]. All symbols are defined in the text. This model of activation barrier is able to account for the essential, qualitative features of the experimental data on both fragile and strong liquids in the sense of the comparisons presented here. Reproduced from [12].

higher activation energy, lying between Q_L and Q_H, is needed to sample the energy landscape. Notice that any formulation that can calculate $Q(T)$ will provide values of the set of four physical parameters (Q_H, Q_L, T_H, T_L). The transition range, between T_L and T_H, may be regarded as the *fragility zone* beyond which the barrier is essentially temperature insensitive. Referring back to Figure 12 one can appreciate the commonality between a strong and a fragile liquid, as well as the different behavior of their respective viscosities. In the particular case of SiO_2 and BLJ, we see the high activation barrier magnitudes are similar, Q_H, ~40–50$k_B T_g$, whereas the low activation barriers are quite different, $Q_L \sim 10 k_B T_g$ (SiO_2) versus $2k_B T_g$ (BLJ). Since Q_H (Q_L) governs the slope $\frac{d\eta}{dT}$ at T_H (T_L), this effect can be seen in Figure 12. The large difference in Q_L also leads to an appreciable difference in the extent of the fragility zone, smaller for SiO_2 than for BLJ, which in turn explains the pronounced fragile behavior of the latter. To explain why Q_L is so much larger for SiO_2 than BLJ, one can examine the activation mechanisms that can be deduced from the relevant atomic configurations [11,12].

A direct consequence of Figure 13 is the existence of two transitions between strong and fragile behavior. For a system at temperatures above T_H its viscosity behavior should be strong since Q is a constant. As T crosses below T_H, a crossover to fragile behavior should occur. With further temperature decrease the system maintains its fragile behavior until T crosses T_L, at which point a second crossover to strong behavior should set in. Thus, two crossovers can be regarded as a universal feature of all glass formers. Extensive experimental evidence for the second crossover has been presented recently [72].

5 Entropy factors and corrections

In our derivation of the network model, equation (11) emerges as an approximation where viscous relaxation can be described by a single effective barrier. We have already remarked that $Q(T)$ has a thermodynamic component in the temperature variation of the average inherent structure, as well as a kinetic component from the TSP trajectory analysis. The connection between the network model and SPA is clearly brought out by equation (10) which shows the former reduces to the latter when there is only one activation path. Thus SPA is a simplification of the network model by ignoring all the correlations (coupling effects) among the different activation paths. One can think of another way to correct the SAP formulation, namely entropy effects. This may be implemented by modifying the activation barrier $Q(T)$ in equation (11) through the introduction of a degeneracy factor $G(T)$ as first suggested by Adam and Gibbs [29],

$$\eta(T) = \eta_0 \exp[Q(T)/\{k_B T \ln G(T)\}]. \qquad (12)$$

One can estimate $G(T)$ from the density of states $G(E_i)$ distribution of the BLJ model following Heuer [29]. Alternatively one can define an energy-dependent entropy $S_c(E) = \ln G(E)$, with E being the inherent structure energy [73]. We have obtained $S_c(E)$ by calculating $G(E)$ from the quench probability distribution $F(E, T)$ [73,74]

$$G(E) \propto F(E, T) \exp(E/k_B T) \qquad (13)$$

Physically, $F(E, T)$ is the probability of the system occupying the inherent structure with energy E at temperature T; it can be determined by performing MD simulations.

We therefore rewrite equation (13),

$$G(E) = G_0(T) F(E, T) \exp(E/k_B T), \qquad (14)$$

where $G_0(T)$ is a temperature-dependent scaling parameter. To obtain $G(E)$ we follow a two-step scaling procedure. First, in Figure 14a we show the results of two MD simulations at two temperatures, T_1 and T_2, with corresponding range of inherent structure energies covered by each distribution.

Using the two distributions we construct a broader distribution by an appropriate choice of $G_0(T)$. The scaling from T_2 to T_1 is indicated by the top arrow in Figure 14b. The combined distribution is an estimate of $G(E)$ to within an unknown constant. The second step in our procedure is to assume there are no inherent structures lying below the lowest value of E in the scaled distribution. Operationally we set $\ln G(E) = 0$ at this lowest value, as indicated in Figure 14c. In this manner we are able to calculate $G(E)$. As a check, we compare our result with that given by Heuer [73,75] after adjusting for different system sizes, 65 atoms in the Heuer study compared to 100 atoms in the present work. One sees agreement between the two results, especially at lower inherent structure energies. Additionally both results follow the Gaussian relation.

Knowing $G(E)$ one can readily evaluate the configurational entropy $S_c(E) = \ln G(E)$, and therefore the entropy correction to the heuristic treatment of the viscosity. The results are shown in Figure 15 [13]. It is clear that the entropy correction effects have an appreciable effect. Judging
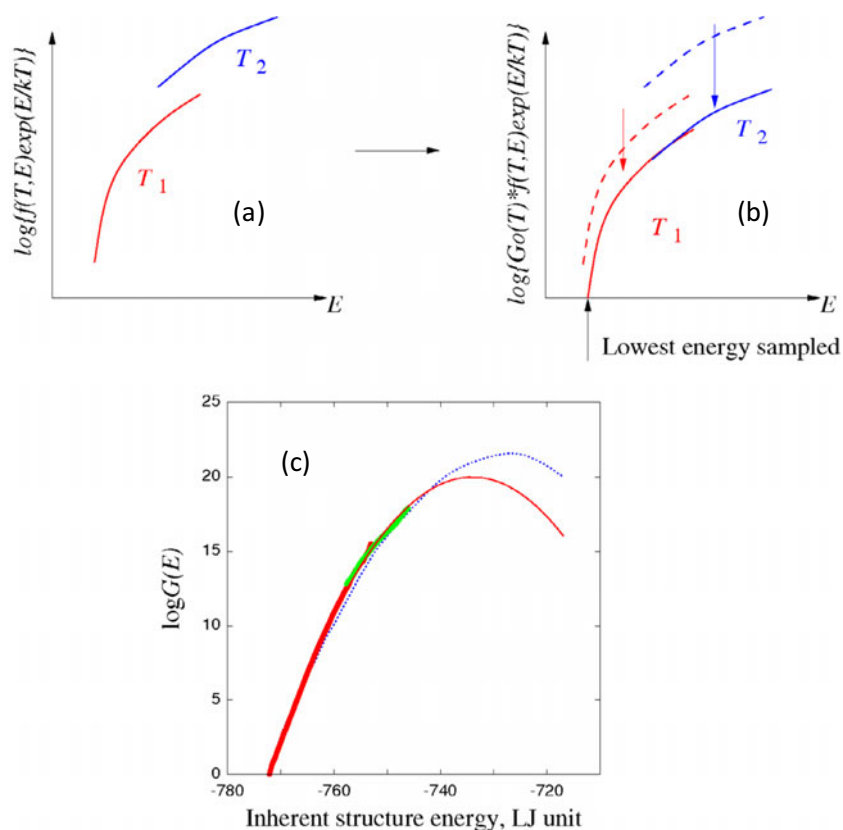
Fig. 14. Schematic illustration showing the scaling procedure described in the text, (a)–(c). The calculated inherent structure distribution $G(E)$ for the potential model BLJ obtained from quench probability at temperature 0.5 and 1.0 are represented by thick red and green lines respectively. Solid (thin) red curve is a Gaussian fit to extend the data. Dotted blue line is the result adapted from [75].

from the present results the effect of configurational entropy is to reduce temperation variation of the activation barrier, a slower increase of the barrier with decreasing temperature, effectively weakening the fragility behavior. With entropy correction estimated in this way the previous heuristic model, equation (11), moves significantly closer to the experimental data (not shown in Fig. 15 but see Fig. 10), as well as the network model calculations. On the basis of Figure 15 it is reaonable to conclude our two formulations are capable of providing a generally satisfactory estimate $\eta(T)$ over the temperatures of interest.

6 Kinetics of defect mobility in solids: activation entropy and Meyer-Neldel compensation

The calculation of $\eta(T)$ is basically a problem of temperature-dependent stress fluctuations where correlations and relaxations in the system are driven by the state variable of temperature. One may consider analogous scenarios of system response to fluctuations driven by an external stress. Atomistic reaction pathway modeling of the kinetics of defect in solids subjected to a stress field is a problem that could be analyzed using
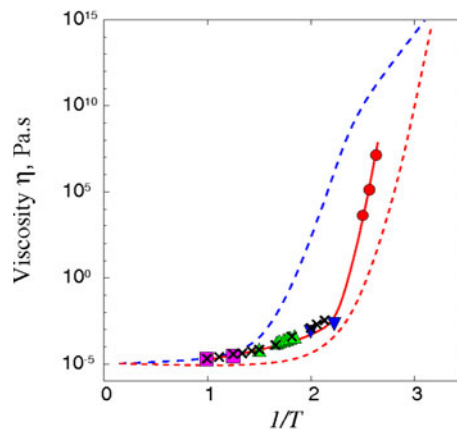
Fig. 15. Effect of entropy correction on the viscosity calculation, heuristic model w/o entropy (blue, dashed), heuristic w/entropy (red, dashed) and the network model (red, solid). The red dots and crosses are results from network model while the other symbols denote MD results of simulations at higher temperatures.

equilibrium TSP sampling. In recent years, extended defects such as dislocations which involve complex collective motion of many atoms [3,76–78] have been studied by combining a solid-state formulation of transition-state

theory [44] with a particular variant of reaction pathway calculations, the free-end nudged elastic band (fe-NEB) method [27,28]. This is another strategy for bridging the laboratory measurements and atomistic modeling of deformation kinetics. The rate-controlling atomic processes can be determined by linking the experimentally measured strain rates with atomistically computed activation energy and volume [28,79]. Examples of application of such a modeling approach to the ultra-strength nanostructured materials have been recently reviewed [3]. In this section, we discuss a critical aspect related to the effect of activation entropy on the kinetic rate estimate, i.e., the pre-exponential factor in the Arrhenius relation. The well-established Meyer-Neldel compensation law [80–82] will be also linked to direct atomistic modeling.

The rate of thermally activated, stress-driven processes can be expressed in a form similar to equation (5),

$$r = N\nu_{MEP}\exp\left(-\frac{\Delta Q(\sigma, T)}{k_B T}\right), \tag{15}$$

where ν_{MEP} is the physical attempt frequency along the MEP (typically about 10^{11}/s), N is the number of equivalent sites of activation, $k_B T$ is the thermal energy, and Q is the activation free energy whose magnitude is controlled by the local stress σ along with the temperature. In the athermal limit we have a critical stress which gives zero activation energy.

The activation free energy $\Delta Q(\sigma, T)$ can be decomposed into

$$\Delta Q(\sigma, T) = \Delta E(\sigma) - T\Delta S(\sigma), \tag{16}$$

where $\Delta E(\sigma)$ is the activation enthalpy that corresponds to the energy difference between the saddle point and initial equilibrium state on the zero-K potential energy surface. Substitution of equation (16) into equation (15) leads to

$$r = \nu\exp\left(-\frac{\Delta E(\sigma)}{k_B T}\right), \tag{17}$$

where

$$\nu = N\nu_{MEP}\exp\left(\frac{\Delta S(\sigma)}{k_B}\right). \tag{18}$$

It should be emphasized that the pre-exponential factor ν_{MEP} in the Arrhenius relation of equation (17) generally varies for different rate processes, and it changes for the same kind of processes under different applied stresses as well. As seen from equation (18), the variation arises due to the change of activation entropy $\Delta S(\sigma)$. There is a well-known empirical Meyer-Neldel (MN) compensation law or iso-kinetic rule [80], which suggests that $\Delta S(\sigma)$ is likely to be correlated with the activation energy,

$$\Delta S(\sigma) = \frac{\Delta E(\sigma)}{T_{MN}}, \tag{19}$$

where T_{MN} denotes the Meyer-Neldel temperature. One may notice the similarity between the present activation entropy and the Adam-Gibbs entropy correction discussed in Section 5.

The role of compensation can be understood as follows: when the applied stress decreases at a constant temperature, the activation energy $\Delta E(\sigma)$ typically increases, causing a decrease of the exponential $\exp\left(-\Delta E(\sigma)/k_B T\right)$. However, according to equation (19), the activation entropy will increase with increasing $\Delta E(\sigma)$, along with ν_0 in equation (18), such that the rate of successful activation ν in equation (17) does not decrease as rapidly as one would expect from only considering the exponential. According to Yelon et al. [83], the MN compensation law has been obeyed in a wide range of kinetic processes, including annealing phenomena, electronic processes in amorphous semi-conductors, trapping in crystalline semi-conductors, conductivity in ionic conductors, aging of insulating polymers, biological death rates, and chemical reactions.

The empirical linear relation between the activation energy and activation entropy in equation (19) is surprisingly simple and effective. Such a remarkable connection has been explained earlier in the context of solid state diffusion, and more generally through the role of multi-excitation entropy [81,82]. Intuitively, the activation process with large activation energy involves the collective motion of a number of atoms. This gives rise to a large number of ways in which the activation can be done through multi-phonon processes, namely a large entropy change between the saddle-point and initial equilibrium state. On the other hand, the increasing number of activated atoms is also manifested through the increase of activation volume, which is defined as

$$\Omega = -\frac{\partial\Delta Q(\sigma, T)}{\partial\sigma}. \tag{20}$$

Ω can be considered to be a kinetic signature of deformation mechanism because it is related to the experimentally measurable strain rate sensitivity m according to $m \sim \frac{k_B T}{\sigma\Omega}$ [3,77]. Substitution of equation (19) into equation (16) gives

$$\Delta Q(\sigma, T) = \Delta E(\sigma)\left(1 - \frac{T}{T_{MN}}\right). \tag{21}$$

This relation furnishes a simple estimate, and interpretation, of the MN temperature T_{MN}. Mott assumed T_{MN} to be the melting temperature of the crystal by noting that the activation free energy $\Delta Q(\sigma, T)$ should approach zero at the melting temperature [84]. This provides an explanation of the large pre-factor of the temperature exponential in the measured rate of grain-boundary slip in pure polycrystalline aluminum. Generally, T_{MN} can be treated as the local melting or disordering temperature.

The above activation entropy effect and the compensation (Meyer-Neldel) law have been investigated by studying the different processes of atomic diffusion on metal surfaces via MD simulations, in particular the importance of activation entropy in a quantitative evaluation of the stress-driven rate processes [16]. Figure 16 shows, as an example, surface dislocation nucleation in a compressed Cu nano-pillar.

In this work, the adaptive strain-boost hyperdynamics [16] was developed to accelerate molecular dynamics
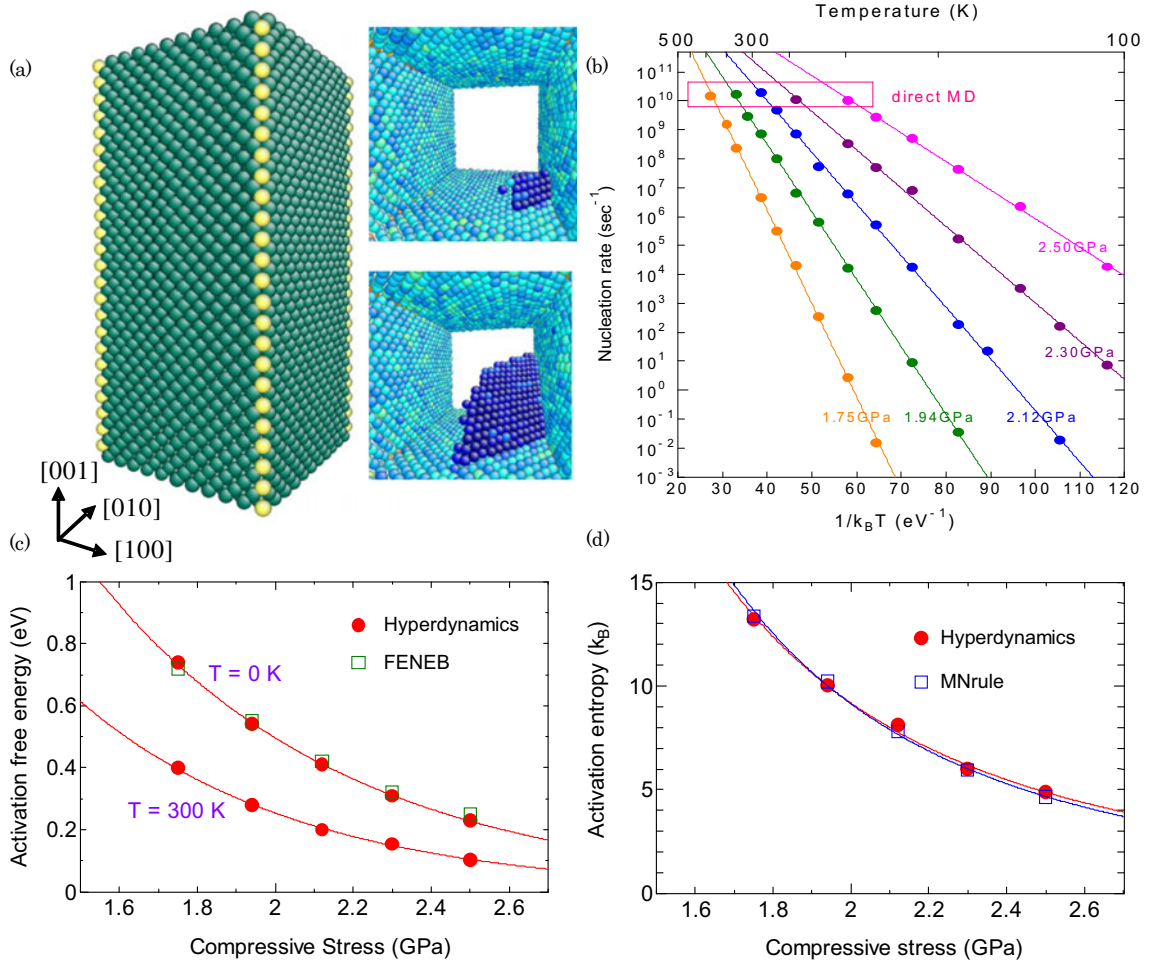
Fig. 16. Atomistic reaction pathway modeling of dislocation nucleation [16]. (a) Atomic configuration of a Cu nano-pillar (left) and typical snapshots of dislocation nucleation from the corner (right). (b) Temperature dependence of the dislocation nucleation rate at different applied stresses from molecular dynamics simulations. (c) Strain-boost hyperdynamics results of stress-dependent activation free energy for dislocation nucleation of (a). For $T = 0$ K case, the comparison with the free-end nudged elastic band results [79] are shown. (d) Activation entropy as a function of stress. The prediction using empirical Meyer-Neldel compensation rule is also presented. Reproduced from [16].

(MD) simulations [7,30]. Figure 16a shows the simulation setup and dislocation nucleation at one of the corners. In Figure 16b, we plot the stress and temperature dependence of the nucleation rate determined from MD. From equations (17) and (18), $\Delta E(\sigma)$ and $\Delta S(\sigma)$ can be determined by the slope and intercept of each curve, respectively. We find that the activation entropy increases as the stress decreases in the stress range of 1.75–2.50 GPa, with typical values between 4–$14k_B$. This means that the saddle-point state is vibrationally more disordered than the initial equilibrium state, due to the presumably softer modes with lower frequency. The result in Figure 16c indicates that, at room temperature, the entropic contribution to the activation free energy is non-negligible and corresponds to about 40% of $\Delta Q(\sigma, T)$ at 0 K. In a previous study of surface dislocation nucleation [79], we conjectured without substantial proof that T_{MN} should be close to the surface disordering temperature, since the local shear resistance should decay to zero when the surface becomes

disordered (pre-melted). Now Figure 16d shows that the classic MN rule gives an excellent prediction of $S(\sigma)$ for the stress range studied with a best fitting parameter of $T_{MN} = 625$ K. The fitted T_{MN} corresponds to nearly half of the bulk melting temperature ($\sim$1350 K) [85], which would be a reasonable guess of surface disordering temperature, and is close to the value of 700 K taken in [79].

Finally, we briefly discuss the nudged elastic band (NEB) method [27] and its novel enhancement [28] for determining the energy barrier of $\Delta E(\sigma)$ in equation (21). The NEB method is a chain-of-states approach for finding the minimum energy path (MEP) and saddle point on the zero-K potential energy landscape. In a NEB calculation, the initial and final states are first determined by local energy minimization. Then a discrete elastic band, consisting of a finite number of replicas of the system, is constructed to connect the two end states. With appropriate relaxation, the band converges to the MEP. The traditional NEB method is effective in searching for the

MEP of localized reactions such as lattice diffusion. However, it is inefficient for studying extended defects in large systems, where the reaction path is typically long and can be highly tilted by stresses. Specifically, in a NEB calculation, the two end-points of the elastic band need to be fixed at two local minima. If the path is long, many intermediate replicas are needed to ensure an appropriate density of nodes on the path; this significantly increases the computational cost when the system is large. On the other hand, if only the initial state (node 0) is a local minimum, but the final state (node N) is not, the band might be shortened without compromising the NEB nodal density. However, the algorithm can behave very badly. This is because if the fixed node N is not chosen to lie exactly on the MEP, node $N-1$ will droop down and end up having much lower energy than node N. In the process, it will drag all the path nodes along due to the spring force, which means that the quality of the NEB mesh degrades with time. An effective way to resolve this issue is to let the final node move, but instead of seeking energy minimization, we require the energy of the final node to stay constant. Thus, node N can only move on the energy iso-surface of, say, -0.5 eV, and the band can swing to improve nodal density around the saddle point, so the saddle point can be efficiently determined. This algorithm, called the free-end NEB method, has been applied to determine the saddle point of dislocation nucleation and migration involving the collective motion of many atoms [28].

7 Atomistic method for slow stress relaxation: thermal creep

In a 2002 paper on creep at very low rates [86], Nabarro wrote in the abstract, "The creep rate in a land-based power station must be less than 10^{-11} s^{-1}", and concluded at the end, "The present state of knowledge reveals specific questions that call for experimental investigation. Theory will contribute, but atomic computation, with a time scale of 10^{-11} s, will not handle processes that take 10^{11} s". One can readily sympathize with this assessment given that molecular dynamics simulation is typically constrained to a time-step size of 10^{-14} s. On the other hand, such a point of view seems to preclude the possibility that methods can be developed to simulate slow dynamical processes without explicitly following all the atomic motions all the time, which is in fact the spirit of multiscale modeling. As described in Section 2, the limitation of MD and related atomistic simulations to probing dynamical processes only on microscopic time scales is long recognized [30]. On the other hand, MD studies of creep deformation have been reported in which one had to resort to high temperature [87], high stress [88], and high strain rate [89]. The underlying problem of extreme strain rates, of the order of 10^7 s^{-1}, remains to date. To reach time scales relevant to creep phenomena one needs to deal with microstructural evolution in the time range from seconds to years. The study of viscosity of deeply supercooled liquids, which we have discussed here, shows this

range of time scales can be reached through TSP sampling techniques. Also, a variation of the ABC and metadynamics algorithms called adaptive boost molecular dynamics simulation [18], where one uses a histogram approach to adaptively construct temperature-dependent boost potential, instead of summation of fixed Gaussians, was shown to be able to model carbon diffusivity in iron, to temperatures that are even lower than in typical experimets.

We now consider whether the activated kinetics of solid-state deformation under stress also can be investigated using the ABC algorithm. That a correspondence should exist between viscous flow and creep is motivated by the notion that all slowly relaxing systems can be described by the elementary processes of activation and relaxation on potential energy landscape. The main difference between applying the ABC algorithm to the problem of viscosity and the problem of solid-state deformation is that the former is concerned with thermal equilibrium under the linear response assumption while the latter pertains to a driven system response under the action of external stresses.

We first consider the process of strain production in two BCC models of nano-grain structures, a 2-D model of columnar grains and a 3-D model of spherical grains. The former is constructed by creating 4 grains of random orientation arranged in a 2 dimensional close packed lattice. The overall periodic box at zero stress has dimensions $39.0 \times 39.0 \times 19.1$ Å and contains 2408 atoms, with the columns oriented along the short axis. The 3-D simulation cell contains 2 grains of random orientation, each 29.8 Å in diameter, and a total of 3456 atoms. A Finnis-Sinclair type empirical potential for Fe is used [15] in the simulations. Both structures are studied at room temperature under uniaxial tension, the 2-D model at 0.1 GPa, and the 3-D model at 0.2 and 0.7 GPa, respectively. A prescribed strain in the z direction is imposed on the initially relaxed system after which energy minimization is performed that involves all the atomic coordinates along the x and y directions. Transition state pathway sampling runs are then conducted with the new cell dimensions held constant.

Figure 17 shows the system set up and trajectory results for the 2-D model. One sees in Figure 17a the system energy evolving toward a lower-energy region during the sampling, while Figure 17c gives the corresponding evolution in the system strain (defined by the deformation of the simulation cell). From the activation energy required by the system to go from one energy minimum to the next, we estimate the time interval associated with each activation process through transition-state theory [44] (also see Eq. (2))

$$t_{A \to B} = \left(\nu \exp \left(-\frac{\Delta E_{A \to B}}{k_B T} \right) \right)^{-1} \qquad (22)$$

where ΔE is the saddle point energy relative to the previous local minimum, ν is a frequency factor (taken to be 10 THz), and T is the temperature. This relation allows us to correlate the strain at any point on the trajectory with a total elapsed time, which is the sum of the individual elapsed times for each preceding activation-relaxation
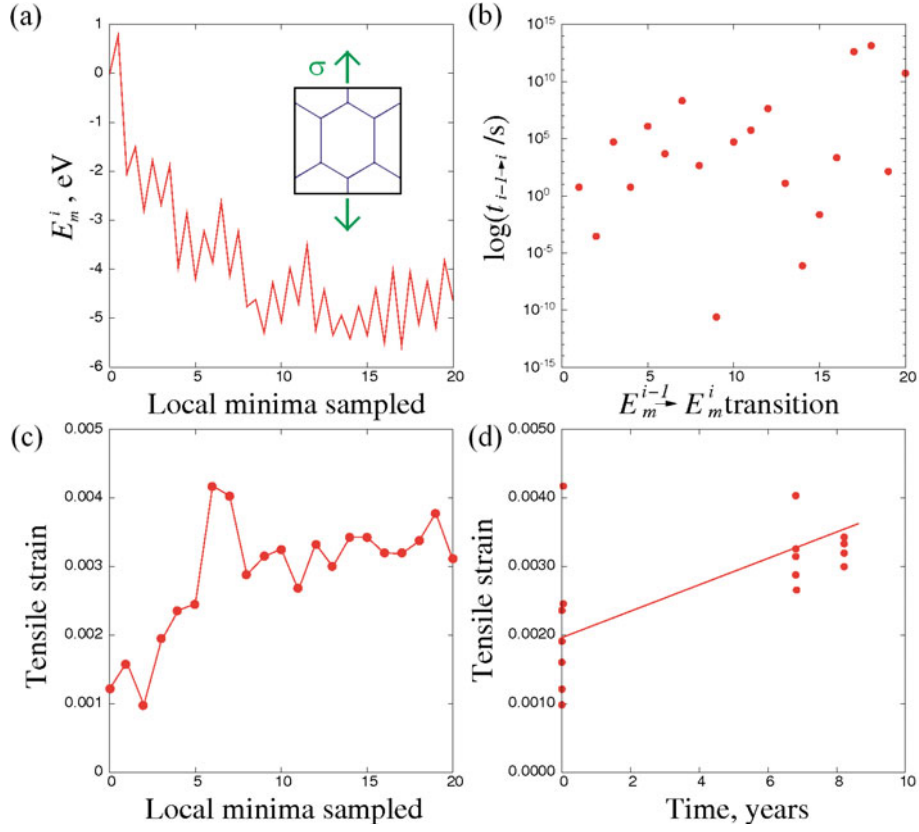
Fig. 17. Determining the strain rate of the columnar grains (2D model) at 0.2 GPa and 300 K. (a) The TSP trajectory. (b) Time needed to move from one minimum to another using equation 21 and $\nu_0 = 10$ THz. (c) System strain along the sampled trajectory. (d) Time evolution of system strain in which the fitted line gives a strain rate of 0.5×10^{-11} s^{-1}. Reproduced from [14].
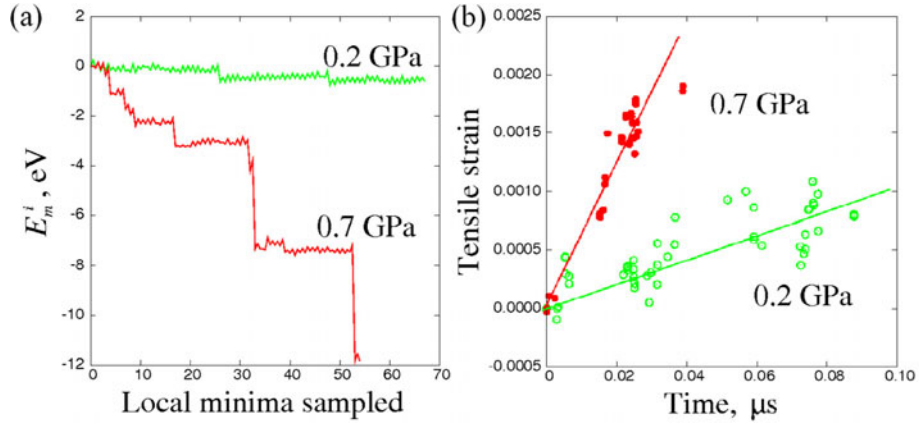
Fig. 18. TSP trajectories of the 3D model at 300K obtained at 0.2 GPa and 0.7 GPa (a), and time evolution of the system strain (b). One may compare these results with those of the 2D model shown in Figure 17. Reproduced from [14].

event along the trajectory. In this way we obtain a strain evolution curve. Implicit in this mapping is the assumption that the individual events are not correlated, which is an often-taken hypothesis in the theory of anelastic deformation [90].

Figure 17d indicates the sampled deformations undergo "fast" transitions (too rapid to resolve on the scale of this figure), except for two slower events, both on the

scale of years. Within any short time interval the data are too scattered to reveal any trend. However, on the long time scale (years) an overall positive trend leads to a strain rate of the order of 10^{-11} s^{-1}, the magnitude previously mentioned by Nabarro as characteristic of macroscopic creep phenomena.

Figure 18 shows the corresponding results obtained for spherical grains (3-D model). A distinctive feature of
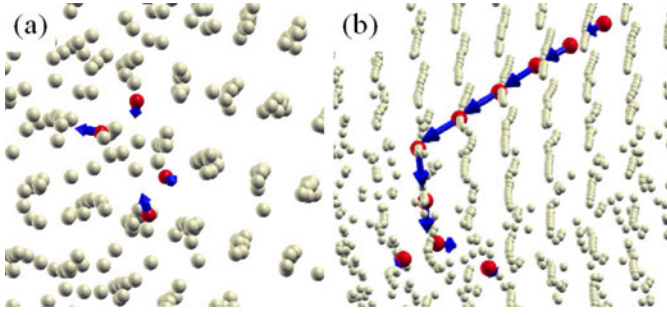
Fig. 19. Atomic displacements in the 3D model, local response within the grain boundary associated with an energy "saw-tooth" (a), and injection of an interstitial atom into the grain boundary, associated with a series of "saw-tooth" and one energy drop (b). Atoms that have displaced more than 0.1 Å or more are marked in red/dark shade. The arrows mark the direction and relative magnitude of displacement. Reproduced from [15].

Figure 18a is the TSP trajectory, with more minima and saddles sampled, showing a series of oscillations, "saw-teeth", punctuated by sudden energy relaxations, particularly pronounced at the higher stress. Figure 18b shows the time evolution of the tensile strain at 300 K from which a strain rate of 1×10^4 s^{-1} at 0.2 GPa and 7×10^4 s^{-1} at 0.7 GPa are estimated.

By analyzing the atomic configurations at selected points along the sampled trajectory one can deduce the characteristic atomic motions associated with a particular system transition. Inspection of the configurations on the two sides of a "saw-tooth" reveals relatively minor local rearrangements within the grain. An example of this type of displacements is shown in Figure 19a. In contrast, inspection of the atomic configurations immediately after an energy drop indicates coordinated displacements that could be regarded as an extended interstitalcy mechanism, eventually leading to a form of grain growth (see Fig. 19b).

We now use transition state theory to estimate the elapsed time for an activation event, and determine a stress relaxation response from the TSP trajectory. In Figure 20 the results are displayed in a log-linear plot. At each applied strain we find the classical behavior of relaxation [91], the transition from an initial state of stress to a final relaxed state over a temporal range that is characterized by a relaxation time. In our results the relaxation extends out to a range of order 10^{15} s. Such a range exceeds typical MD capability by some 20 orders of magnitude; it is also 12 orders of magnitude beyond the 1000-second scale of mechanical spectroscopy measurements [90]. Additionally the simulations show the relaxation process, roughly characterized by the position of the "knee" in the relaxation curve, slows down significantly with increasing strain. An effective relaxation time τ can be extracted by fitting the simulations to a traditional empirical expression [92]

$$\frac{\sigma(t)}{\varepsilon_0} = M_R + (M_U - M_R)\exp\left(-\frac{t}{\tau}\right), \qquad (23)$$
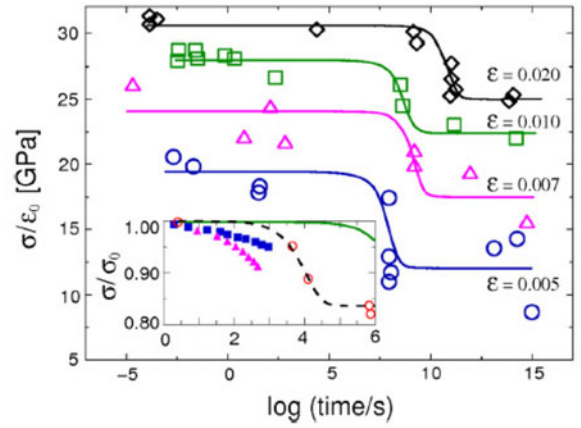

Fig. 20. Temporal evolution of von Mises stresses at 400 K and various applied strains [15]. Each data represents a weighted average of the calculated stress within a 0.01 interval of log (time/s). Solid curves are results of fitting. Inset shows comparison of experimental data at strains of 0.0002 for two samples, "as prepared" (triangles) and "annealed" (squares) at 313 K and 408 K respectively, with simulation results of the pristine nanocrystal (solid line) and the distributed-vacancy (dashed line) models at 400 K. Reproduced from [15].

where ε_0 is the constant applied strain, M_R and M_U are the relaxed and unrelaxed stresses respectively.

A more contemporary description of relaxation in complex systems would be to replace the simple exponential in equation (23) by a stretched exponential, $\exp\left[-(t/\tau)^\beta\right]$, also known as the Kohlrausch function. For example, the decay of density fluctuations in the dynamics of glassy liquids, the so-called alpha relaxation, is well represented by such an expression [20,61,93], with the Kohlrausch exponent β ranging from 1 to 0.7. Fitting the simulation data at 0.020 strain in this manner gives $\beta \sim 0.4$ for stress relaxation in our particular nanocrystalline model. The implication is that this is a concerted relaxation process involving a broad distribution of strain-activated events.

The significant effect of the applied strain on the stress relaxations is quite visible in Figure 21a, with larger energy drops occurring at higher strains. This is understandable from the fact that the energy penalty for "backwards" microstructural evolution during stress-relaxation should be higher at higher strains. Secondly, the number of saw-tooth oscillations in between the relaxations is seen to be reduced. In terms of the corresponding atomic displacements, we find the applied strain does not affect the general character of the individual transitions, whereas it does have an overall effect on how extended are the corresponding atomic displacements throughout the system, see Figures 21b and 21c. At the higher strain the number of participating sites is more widely distributed. A more efficient probing of the "weak spots" is consistent with the observed decrease in the number of saw-tooth oscillations between energy-drop events. Such behavior clearly illustrates the difficulty of dealing with deformation at extreme strain rates in conventional MD simulations. If
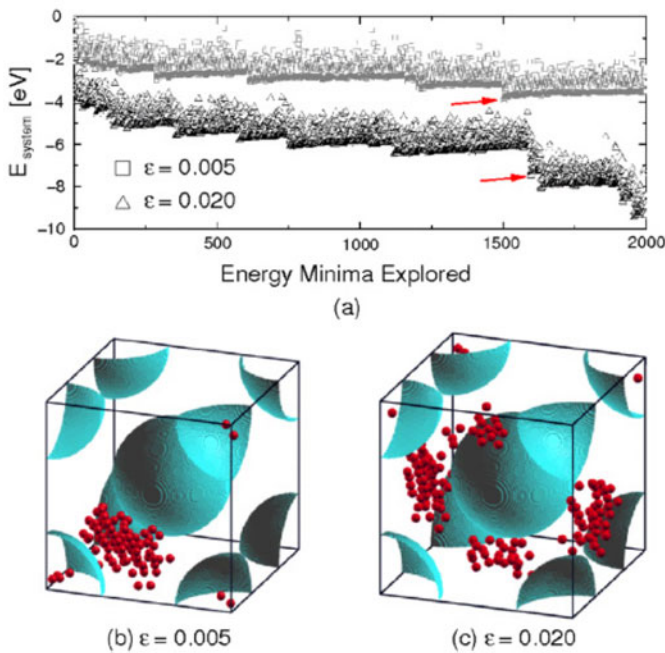
Fig. 21. TSP trajectories sampled at applied strains of 0.005 and 0.02 by ABC (a), and atomic configurations associated with the energy drop event at 0.005 strain (indicated by the arrow in (a)) showing cluster of atoms that have undergone displacements greater than 0.1 A during the event (b). (c) Same as (b) except for strain 0.02. Reproduced from [15].

the applied driving force is unphysically large, one cannot hope to resolve the individual processes of interest because many transitions are simultaneously activated.

8 Discussion and outlook

We have seen transition state pathways can be sampled to gain atomic-level insights into the dynamics of slow relaxation in supercooled liquids. As a result the temperature variation of the shear viscosity over several decades can be explained using basic interatomic interaction models. That this approach can describe the strong and fragile scaling of a variety of glass forming liquids should be noteworthy in the current discussions on the nature of the glass transition. In this active area of statistical mechanics research there is no shortage of novel algorithms and atomistic simulation techniques that have been suggested in the literature. While we have found the ABC algorithm to be sufficiently robust for inherent structure sampling, the transition state pathway sampled may not be as accurate as other methods such as NEB. This is a topic suitable for further study. One can imagine devising a hybrid scheme using ABC to map out an extended trajectory segment and NEB to determine the saddles more accurately. Such an approach has been used recently to study void nucleation in an irradiated metal brought about by vacancy clustering and cluster coalescence [17]. By combining ABC with NEB and kinetic Monte Carlo to inves-

tigate the evolution of small vacancy clusters in bcc Fe, an accelerated growth mechanism was obtained at a transition temperature in agreement with the value observed by positron annihilation spectroscopy measurements. In the ABC algorithm implemented here the system evolves on a time-independent energy surface, that is, the system is not driven by a time-dependent external field. One could imagine formulating a dynamic version of ABC for system evolutions occurring on time scales comparable to the time scales of external perturbations [94]. An example of this situation could be the problem of radiation damage accumulation during the operation of a nuclear reactor.

We have found in both the viscosity and creep studies the analysis of atomic configurations associated with a specific (isolated) event on the TSP trajectory can give insights on cooperative displacements of a few particles and atomic-level mechanisms of activation and relaxation. In the viscosity problem, we have looked for changes in the atomic displacements associated with three characteristic barrier-climbing events, and found that low-Q activation involves only a few atoms, while at higher Q, chain-like collective displacements can be seen, and at even higher Q the rearrangements return to a more extended but isotropic distribution [11]. Although these are limited results, they appear to be consistent with recent notions of hopping between PES metabasins [75,95]. Information of this kind, when combined with topographical features of the TSP trajectory, could lead to broader understanding of the kinetics of slow system evolution. Further work along this direction would be worthwhile.

Using the ABC method to study stress (creep) relaxation in a model nanocrystal, we demonstrate an atomistic approach to probing macroscopic time scales, while also providing access to atomic configuration details. We uncover an underlying mechanism involving discrete, localized irreversible atomic displacements. These appear to be the unit process previously observed in molecular dynamics simulations at strain rates many orders of magnitude higher. We also find experimental test of creep simulations requires the availability of specimens with microstructure imperfections effectively matching those of the simulation. With the recent advances in high-resolution measurement techniques, such as field ion beam fabrication of nanopillars and nano-indentation measurement of small-scale yielding, a new class of experiments is thus suggested. One can look forward to experiments coupling nanoscale plastic deformation measurements with predictive atomistic simulations [96,97] extended to include TSP sampling methods such as ABC.

We return to the theme of this work which is slow dynamics from the standpoint of atomistic simulation. Now that we have seen using atomistic reaction path sampling to gain understanding of glassy kinetics and slow stress relaxation, we might consider other materials phenomena which may be similarly studied. But first one may ask what qualifies as slow dynamics. We have implicitly taken glass viscosity and creep to be phenomena of slow dynamics. The connection between viscosity and time evolution can be seen from the visco-elastic form of defining $\eta(T)$,
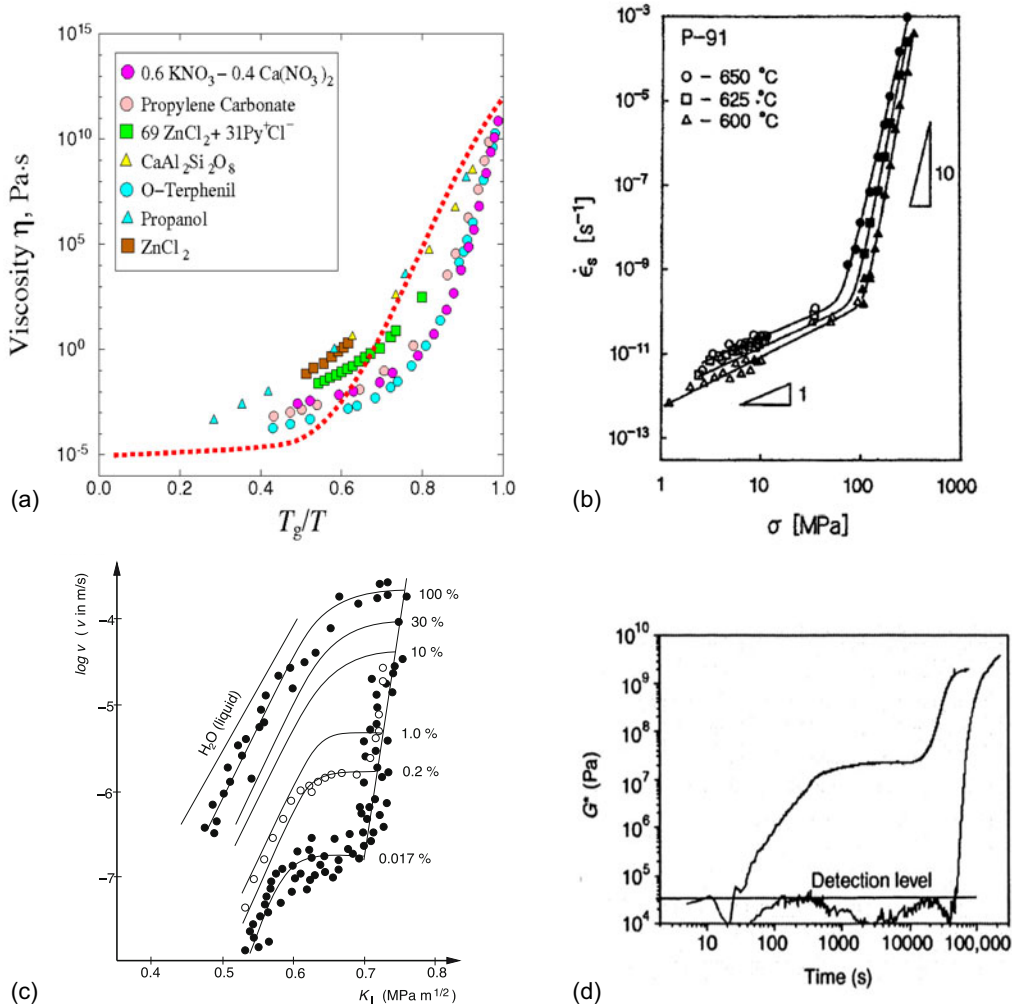
Fig. 22. A collection of materials behavior illustrating the defining character of slow dynamics. (a) Temperature variation of shear viscosity of supercooled liquids [22], (b) stress variation of strain rate in P-91 steel [104], (c) stress loading variation of crack speed in soda-lime (NaOH) glass at various humidity [105], (d) time variation of shear modulus in hardening of Portland cement paste (water/cement ratio of 0.8) measured by ultrasound propagation [106].

$\eta(T) = G\tau(T)$, where G is the shear modulus and τ the shear relaxation time (recall discussion of Eq. (8)). Since supercooled liquids or glasses have very large viscosities (Sect. 4), it means these systems exhibit very long relaxation times. If we take $\eta \sim 10^{12}$ Pa s and $G \sim 10^{10}$ Pa, then we get a typical relaxation time τ of 100 s. In the case of creep we have seen (Sect. 8) that deforming crystalline solids with limited defect content can undergo very slow stress or strain relaxations. However, not all systems with long relaxation times are necessarily good candidates for atomistic simulation studies. More experience with the use of algorithms like ABC in problems like viscosity and creep is needed to expand our insights into how complex microstructures evolve over long times.

We show in Figure 22 three selected functional behavior of materials, creep in a metal, stress corrosion cracking in a glass, and the hardening of cement paste. Each is a characteristic of a complex materials phenomenon of con-

siderable technological importance. Yet it is seldom that they are discussed from a common point of view. Our motivation in displaying them along side of the shear viscosity of supercooled liquids is to suggest that slow dynamics is ubiquitous in the evolution of complex systems.

The variation of strain-rate with stress and temperature, seen in Figure 22b, is a conventional way to characterize structural deformation [91]. Notice the similar appearance between Figures 22a and 22b, where the data are plotted against inverse temperature and stress, respectively. The presence of two distinct stages of variation may be taken to indicate two competing atomic-level responses. In the viscosity case we know the high-T regime of small η and the low-T stage of large η are governed by continuous collision dynamics, well described by the mode coupling theory [93] and barrier hopping (see Sect. 4), respectively. One may expect analogous interplay between dynamical processes occurring at different spatial and temporal scales

in the case of stress-driven creep. The two corresponding stages are a low-stress strain rate, usually analyzed through a power law exponent, and a high-stress high strain rate regime. Attempts to explain creep on the basis of atomic-level mechanism of dislocation climb are in its infancy [98]; TSP methods such as ABC could prove useful as suggested by a recent study of self-interstitial clusters [99]

Viscosity and creep are phenomena where the system microstructure evolves through cooperative rearrangements or lattice defect interactions without chemical (compositional or stoichiometric) changes. In contrast the stress variation of the crack velocity, Figure 22c, shows the classic three-stage behavior of stress corrosion cracking (SCC) [100]. One can distinguish in the data a corrosion-dominated regime at low stress (stage I), followed by a plateau (stage II) where the crack maintains its velocity with increasing stress, and the onset of a rapid rise at high stress (stage III) where stress effects now have a dominant role. Relative to Figures 22a and 22b, the implication here is that a complete understanding of SCC requires an approach where chemistry (corrosion) and stress effects are treated on equal footing. Atomistic studies of water reaction with silica, the problem of hydrolytic weakening well known in geo-science, have been attempted using NEB [101]. The extension of ABC to reactions involving bond breaking and formation, which have been previously studied by molecular dynamics simulation is another area for further work.

A further reason for showing the different behavior together in Figure 22 is to draw attention to a progression of microstructure evolution complexity, from viscosity to creep, to SCC, and to cement setting. In Figure 22d one sees another classic 3-stage behavior in the hardening of cement paste. The hydration or setting curve is known to everyone in the cement science community, on the other hand a satisfactory explanation in terms of molecular mechanisms is lacking [102]. A microstructure model of calcium-silicate-hydrate, the binder phase of cement, has been recently established [103] which could serve as starting point for the study of viscosity, creep deformation, and even the setting characteristics of cement [94]. If viscosity or glassy dynamics is the beginning of this progression where the challenge lies in the area of statistical mechanics, followed by creep in the area of solid mechanics (mechanics of materials), then SCC and cement setting may be regarded as future challenges in the emerging area of chemo-mechanics [101,107]. The understanding of the role of stage II in the latter phenomena could be an interesting topic by itself.

The present discussion of viscous relaxation and creep deformation may be considered an extension of the applications of metadynamics-based reaction pathway sampling to flow and deformation of matter driven by thermal and stress fluctuations, in addition to the existing chemical and biomolecule applications. It seems clear that the issues of materials ageing and degradation in extreme environments have a great deal of fundamental commonality across physical and biological systems. Because of

this, simulation-based concepts and algorithms that allow one to understand temporal evolution at the systems level in terms of molecular interactions and cooperativity are likely to be of enduring interest.

References

1. S. Yip, Nat. Mater. **2**, 3 (2003)
2. *Handbook of Materials Modeling*, edited by S. Yip (Springer, New York, 2005)
3. T. Zhu, J. Li, Prog. Mater. Sci. **55**, 710 (2010)
4. Y.Z. Wang, J. Li, Acta Mater. **58**, 1212 (2010)
5. US-NSF, *Blue Ribbon Panel on Simulation-Based Engineering Science* (2006)
6. US-DOE, *Decadal Challenges for Predicting and Controlling Materials Performance in Extremes* (Los Alamos National Laboratory, 2010)
7. A.F. Voter, Phys. Rev. Lett. **78**, 3908 (1997)
8. A. Laio, M. Parrinello, Proc. Natl. Acad. Sci. USA **99**, 12562 (2002)
9. A. Laio, F.L. Gervasio, Rep. Prog. Phys. **71**, 126601 (2008)
10. A. Barducci, M. Bonomi, M. Parrinello, in WIREs. Comput. Mol. Sci., `wires.wiley.com/wcms`, Jan.–Feb. 1 (2011)
11. A. Kushima, X. Lin, J. Li, J. Eapen, J.C. Mauro, X. Qian, P. Diep, S. Yip, J. Chem. Phys. **130**, 224504 (2009)
12. A. Kushima, X. Lin, J. Li, X. Qian, J. Eapen, J.C. Mauro, P. Diep, S. Yip, J. Chem. Phys. **131**, 164505 (2009)
13. J. Li, A. Kushima, J. Eapen, X. Lin, X. Qian, J.C. Mauro, P. Diep, S. Yip, PLoS ONE **6**, e17909 (2011)
14. T.T. Lau, A. Kushima, S. Yip, IOP Conference Series Materials Science and Engineering **3**, 012002 (2009)
15. T.T. Lau, A. Kushima, S. Yip, Phys. Rev. Lett. **104**, 175501 (2010)
16. S. Hara, J. Li, Phys. Rev. B **82**, 184114 (2010)
17. Y. Fan, A. Kushima, S. Yip, B. Yildiz, Phys. Rev. Lett. **106**, 125501 (2011)
18. A. Ishii, S. Ogata, H. Kimizuka, J. Li, Adaptive boost molecular dynamics simulation of carbon diffusion in iron, to be published (2011)
19. C.A. Angell, Science **267**, 1924 (1995)
20. S. Sastry, P.G. Debenedetti, F.H. Stillinger, Nature **393**, 554 (1998)
21. P.G. Debenedetti, F.H. Stillinger, Nature **410**, 259 (2001)

22. C.A. Angell, J. Phys. Chem. Solids **49**, 863 (1988)

23. J.C. Dyre, Rev. Mod. Phys. **78**, 953 (2006)

24. K. Trachenko, V.V. Brazhkin, J. Phys.: Condens. Matter **21**, 425104 (2009)

25. J. Li, Mater. Res. Soc. Bulletin **32**, 151 (2007)

26. J.D. Eshelby, Proc. R. Soc. Lond. A **241**, 376 (1957)

27. H. Jónsson, G. Mills, K.W. Jacobsen, *Classical and Quantum Dynamics in Condensed Phase Simulations*, edited by B.J. Berne, G. Ciccotti, D.F. Coker (World Scientific, 1998)

28. T. Zhu, J. Li, A. Samanta, H.G. Kim, S. Suresh, Proc. Natl. Acad. Sci. USA **104**, 3031 (2007)

29. A. Heuer, J. Phys.: Condens. Matter **20**, 373101 (2008)

30. A.F. Voter, F. Montalenti, T.C. Germann, Ann. Rev. Mater. Res. **32**, 321 (2002)

31. M. Goldstein, J. Chem. Phys. **51**, 3728 (1969)

32. D.J. Wales, *Energy Landscapes* (Cambridge University Press, Cambridge, 2003)

33. F.H. Stillinger, T.A. Weber, Phys. Rev. A **25**, 978 (1982)

34. F.H. Stillinger, T.A. Weber, Science **225**, 983 (1984)

35. F. Sciortino, J. Stat. Mech. P05015 (2005)

36. G.M. Torrie, J.P. Valleau, J. Comput. Phys. **23**, 187 (1977)

37. T. Huber, A.E. Torda, W.F. Gunsteren, J. Comput. Aided Mol. Design **8**, 695 (1994)

38. E. Marinari, G. Parisi, Europhys. Lett. **19**, 451 (1992)

39. E. Darve, A. Pohorille, J. Chem. Phys. **115**, 9169 (2001)

40. D. Rodriguez-Gomez, E. Darve, A. Pohorille, J. Chem. Phys. **120**, 3563 (2004)

41. F. Wang, D.P. Landau, Phys. Rev. E **64**, 056101 (2001)

42. H. Grubmüller, Phys. Rev. E **52**, 2893 (1995)

43. H. Eyring, J. Chem. Phys. **3**, 107 (1935)

44. G.H. Vineyard, J. Phys. Chem. Solids **3**, 121 (1957)

45. B.P. Uberuaga, R.G. Hoagland, A.F. Voter, S.M. Valone, Phys. Rev. Lett. **99**, 135501 (2007)

46. G. Henkelman, H. Jonsson, J. Chem. Phys. **111**, 7010 (1999)

47. G.T. Barkema, N. Mousseau, Phys. Rev. Lett. **77**, 4358 (1996)

48. D.W. Marquardt, J. Soc. Indust. Appl. Math. **11**, 431 (1963)

49. R.A. Miron, K.A. Fichthorn, J. Chem. Phys. **119**, 6210 (2003)

50. L.Y. Chen, N.J.M. Horing, J. Chem. Phys. **126**, 224103 (2007)

51. G. Bussi, A. Laio, M. Parrinello, Phys. Rev. Lett. **96**, 090601 (2006)

52. P.G. Kevrekidis, C. Theodoropoulos, I.G. Kevrekidis, O. Runborg, J.M. Hyman, C.W. Gear, Comm. Math. Sci. **1**, 715 (2003)

53. I.G. Kevrekidis, C.W. Gear, G. Hummer, AIChE J. **50**, 1346 (2004)

54. D. Donadio, P. Raiteri, M. Parrinello, J. Phys. Chem. B **109**, 5421 (2005)

55. F. Trudu, D. Donadio, M. Parrinello, Phys. Rev. Lett. **97**, 105701 (2006)

56. C. Michel, A. Laio, A. Milet, J. Chem. Theory Comput. **5**, 2193 (2009)

57. G.A. Tribello, M. Ceriotti, M. Parrinello, Proc. Natl. Acad. Sci. USA **107**, 17509 (2010)

58. P.J. Feibelman, Phys. Rev. Lett. **65**, 729 (1990)

59. G. Henkelman, G. Jóhannesson, H. Jónsson, *Progress on Theoretical Chemistry and Physics*, edited by S.D. Schwartz (Kluwer Academic, Dordrecht, 2000), pp. 269–300

60. D. Passerone, M. Parrinello, Phys. Rev. Lett. **87**, 108302 (2001)

61. W. Kob, H.C. Andersen, Phys. Rev. E **52**, 4134 (1995)

62. W. Kob, H.C. Andersen, Phys. Rev. E **51**, 4626 (1995)

63. O.M. Becker, M. Karplus, J. Chem. Phys. **106**, 1495 (1997)

64. J.C. Dyre, Nat. Mater. **3**, 749 (2004)

65. D.A. McQuarrie, *Statistical Mechanics* (University Science Books, 2000)

66. J.P. Boon, S. Yip, *Molecular Hydrodynamics* (Dover, New York, 1991)

67. A. Baronchelli, A. Barrat, R. Pastor-Satorras, Phys. Rev. E **80** (2009)

68. P. Moretti, A. Baronchelli, A. Barrat, R. Pastor-Satorras, J. Stat. Mech., P03032 (2011)

69. B. Coluzzi, G. Parisi, P. Verrocchio, J. Chem. Phys. **112**, 2933 (2000)

70. C. Rehwald, O. Rubner, A. Heuer, Phys. Rev. Lett. **105**, 117801 (2010)

71. W. Kob, C. Donati, S.J. Plimpton, P.H. Poole, S.C. Glotzer, Phys. Rev. Lett. **79**, 2827 (1997)

72. F. Mallamace, C. Branca, C. Corsaro, N. Leone, J. Spooren, S.-H. Chen, H.E. Stanley, Proc. Natl. Acad. Sci. USA **107**, 22457 (2010)

73. A. Heuer, J. Phys.: Condens. Matter **20**, 373101 (2008)

74. J.C. Mauro, R.J. Loucks, J. Balakrishnan, S. Raghavan, J. Chem. Phys. **126**, 194103 (2007)

75. B. Doliwa, A. Heuer, Phys. Rev. E **67**, 031506 (2003)

76. Y. Mishin, M. Asta, J. Li, Acta Mater. **58**, 1117 (2010)

77. J. Li, Mater. Res. Soc. Bulletin **32**, 151 (2007)

78. T. Zhu, J. Li, S. Ogata, S. Yip, Mater. Res. Soc. Bulletin **34**, 167 (2009)

79. T. Zhu, J. Li, A. Samanta, A. Leach, K. Gall, Phys. Rev. Lett. **100**, 025502 (2008)

80. W. Meyer, H. Neldel, Z. Tech. Phys. **12**, 588 (1937)

81. A. Yelon, B. Movaghar, Phys. Rev. Lett. **65**, 618 (1990)

82. A. Yelon, B. Movaghar, R.S. Crandall, Rep. Prog. Phys. **69**, 1145 (2006)

83. A. Yelon, B. Movaghar, H.M. Branz, Phys. Rev. B **46**, 12244 (1992)

84. N.F. Mott, Proc. Phys. Soc. Lond. **60**, 391 (1948)

85. T. Frolov, Y. Mishin, Phys. Rev. B **79**, 045430 (2009)

86. F.R.N. Nabarro, Metall. Mater. Trans. A **33**, 213 (2002)

87. V. Yamakov, D. Wolf, S.R. Phillpot, H. Gleiter, Acta Mater. **50**, 61 (2002)

88. H. Van Swygenhoven, M. Spaczer, A. Caro, D. Farkas, Phys. Rev. B **60**, 22 (1999)
89. J. Schiøtz, T. Vegge, F.D.D. Tolla, K.W. Jacobsen, Phys. Rev. B **60**, 11971 (1999)
90. E. Bonetti, E.G. Campari, L. Del Bianco, L. Pasquini, E. Sampaolesi, Nanostruct. Mater. **11**, 709 (1999)
91. M.E. Kassner, *Fundamentals of Creep in Metals and Alloys*, 2nd edn. (Elsevier, Amsterdam, 2009)
92. A.S. Nowick, B.S. Berry, *Anelastic Relaxation in Crystalline Solids* (Academic Press, New York, 1972)
93. W. Götze, *Complex Dynamics of Glass Florming Liquids* (Oxford University Press, Oxford, 2009)
94. P.R. Monasterio, *Multiscale Modeling of Slow Dynamical Processes*. Ph.D. thesis, MIT, 2010
95. G.A. Appignanesi, J.A. Rodriguez, R.A.M. Fris, W. Kob, Phys. Rev. Lett. **96**, 057801 (2006)
96. C.R. Weinberger, W. Cai, Proc. Natl. Acad. Sci. USA **105**, 14304 (2008)
97. C.R. Weinberger, W. Cai, Nano Lett. **10**, 139 (2010)
98. M. Kabir, T.T. Lau, D. Rodney, S. Yip, K.J. Van Vliet, Phys. Rev. Lett. **105**, 095501 (2010)
99. Y. Fan, A. Kushima, B. Yildiz, Phys. Rev. B **81**, 104102 (2010)
100. M. Ciccotti, J. Phys. D Appl. Phys. **42**, 214006 (2009)
101. T. Zhu, J. Li, X. Lin, S. Yip, J. Mech. Phys. Solids **53**, 1597 (2005)
102. J.W. Bullard, H.M. Jennings, R.A. Livingston, A. Nonat, G.W. Scherer, J.S. Schweitzer, K.L. Scrivener, J.J. Thomas, Cem. Concr. Res., in Press, Corrected Proof
103. R.J.M. Pellenq, A. Kushima, R. Shahsavari, K.J. Van Vliet, M.J. Buehler, S. Yip, F.J. Ulm, Proc. Natl. Acad. Sci. USA **106**, 16102 (2009)
104. R.L. Klueh, Int. Mat. Rev. **50**, 287 (2005)
105. S.M. Wiederhorn, J. Am. Ceram. Soc. **50**, 407 (1967)
106. D. Lootens, P. Hebraud, E. Lecolier, H.V. Damme, Oil Gas Sci. Technol. Rev. IFP **59**, 31 (2004)
107. K.J. Van Vliet, Sci. Model. Simul. **15**, 67 (2008)